Numerical Analysis on Free Convection and Mass Transfer Phenomena in Electrochemical System

Shunsuke Kawai

2009

ABSTRACT

We examine how the nonuniform distribution of current density develops along the electrode surface in confined electrochemical system. For this purpose, we numerically study free convection and mass transfer accompanying the electrochemical reactions on the electrode surface immersed in an aqueous electrolyte solution. Two-dimensional numerical simulation is performed for copper electrolysis in an aqueous copper sulfate ($CuSO_4$) electrolyte solution sandwiched by the two vertical plane electrodes. We focus on the dependence of vertical nonuniformity of current density distribution on mass transfer associated with free convection. The development mechanism of free convection is investigated for a particular case of the applied current density of 2 mA/cm^2 and the electrode spacing of 2 mm. A steady state is realized at large times. A single swirling motion compatible with the buoyant flow is observed along the electrode and wall surfaces at the steady state. It is confined to the thin boundary layer and the interior region stays almost stagnant. A heavier (or lighter) electrolyte solution is transferred to the lower cathode (or upper anode) region by this rotational flow. The supply of concentration from the counter electrode causes nonuniform current density distribution along the vertical direction. By changing the applied current density or the electrode spacing, we find that as the applied current density increases, current density distribution becomes more nonuniform by the stronger rotational fluid motion. As the electrode spacing decreases, more nonuniform distribution of current density is attained earlier, even though the steady swirling flow gets weaker.

Contents

Section 1 Introduction

There exist many electrochemical systems in our daily lives, such as the metal electroplating, primary and secondary batteries, copper wiring technique in the microprocessor and graphic chip, and the electrochemical pattern etching in electronic circuit design. In these systems, we know that the electrochemical deposition and dissolution reactions of metal on the electrode surface are essential phenomena. It is thus indispensable to understand and control the electrochemical reactions, which may improve the efficiency and productivity in battery systems and electrolytic tankhouse.

The electrolytic refining and winning processes have been widely adopted as the extraction method of high purity metals such as copper, silver, gold, and zinc. The current industrial copper electrolytic tankhouse commonly consists of many electrode arrays, where 1 meter high vertical plane electrode surfaces are placed face to face, separated by a 0.01-0.1 meters thick electrolyte solution layer. On the other hand, with the great progress in microelectronics, especially motivated by the successful application of Damascene process in IBM [1], the electrochemical method to fill trench or pore with metal has attracted much more attention [2-5]. The feature scale of the trench is the order of 10^{-7}-10^{-4} meters and the aspect ratio is generally within 0.1 to 10.

Figure 1.1 shows the relationships between the aspect ratio B (see Eq. (2-38) for definition) and the applied average current density j_{ave} frequently employed in several industrial copper electrochemical systems. In this figure, the "Region IV" represents the parameter region where some functional materials such as copper nanotube, nanowire, and nanoparticle have been fabricated by the electrochemical method in the laboratory level.

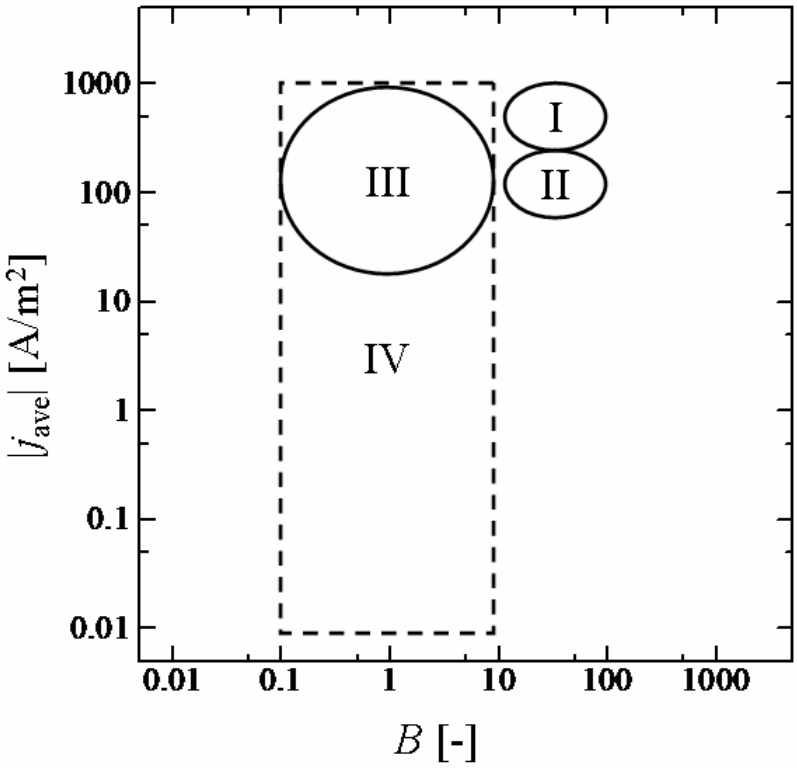

Figure 1.1: Relationship between the aspect ratio B and the applied average current density j_{ave} in several industrial copper electrochemical systems. Region I: Copper electrorefining system [6-a, 7], Region II: Copper electrowining system [6-b], Region III: Trench filling and pattern etching by electrochemical method [8-15], Region IV: Laboratory level electrochemical material tailoring research.

It is clearly seen that the electrochemical systems have a broad range of B and j_{ave}, and the operational electrolytic condition varies widely depending on the intended use.

The optimal designing of operational electrolytic condition is indispensable to improve the industrial productivity. The high electrolytic current operation is desired

because the productivity is proportional to the applied electrolytic current. However, it is well-known that the current density distribution readily becomes nonuniform when a high electric current is applied. The dendritic or needle-like electrodeposited metal growth and unwanted side reactions are possibly induced. As a result, the high electric current operation causes the nonuniform electrolytic metal film in the electrorefining and winning systems. Besides, it produces the void in the electrochemical trench filling, which results in the breakdown and degradation of copper wiring. It is required to profoundly understand the development mechanism of the nonuniform current density distribution along the electrode surface.

So far many theoretical and numerical studies have been carried out on mass transfer phenomena accompanying the electrochemical reactions, since Wagner's pioneering work [16]. However, most studies have employed the boundary layer theory in semi-infinite media, and only two extreme cases of boundary condition on the electrode surface have been discussed. One is the uniform current density along the electrode surface, which is realized when the applied electrolytic current is sufficiently low [17-21]. The other is the zero concentration of a reactant species on the electrode surface when the applied electrolytic current is extremely high [16-23]. Even in recent studies of confined electrochemical system [24-28], the above-mentioned simplified boundary conditions are imposed on the electrode surface. Therefore, it is still unsolved how the current density distribution develops along the electrode surface.

The aim of this study is to examine the development mechanism of current density distribution along the electrode surface. Whence, we study free convection and mass transfer caused by the electrochemical reactions in confined electrochemical system. In particular, we focus on the dependence of the vertical current density

distribution on mass transfer associated with free convections developing along the vertical plane electrodes immersed in a stagnant aqueous electrolyte solution. In Section 2, a mathematical model is developed in a binary aqueous electrolyte solution system. The governing equations are described by the mass and momentum conservation equations, in which the buoyancy effect is accounted through the Boussinesq approximation. The boundary condition modeling is based on the electrochemistry, where the dilute-solution theory for ion transport is employed. In Section 3, two-dimensional numerical simulation is carried out for copper electrolysis in an aqueous copper sulfate ($CuSO_4$) electrolyte solution as a model case. A summary of this study is given in Section 4.

Section 2 Mathematical Model and Calculation Procedure

2.1 Problem Statement

In this section, a mathematical model is developed in a binary aqueous electrolyte solution system. Figure 2.1 shows the geometry of the two-dimensional (2D) container filled with a dilute aqueous electrolyte solution to be considered, where the coordinate system is defined.

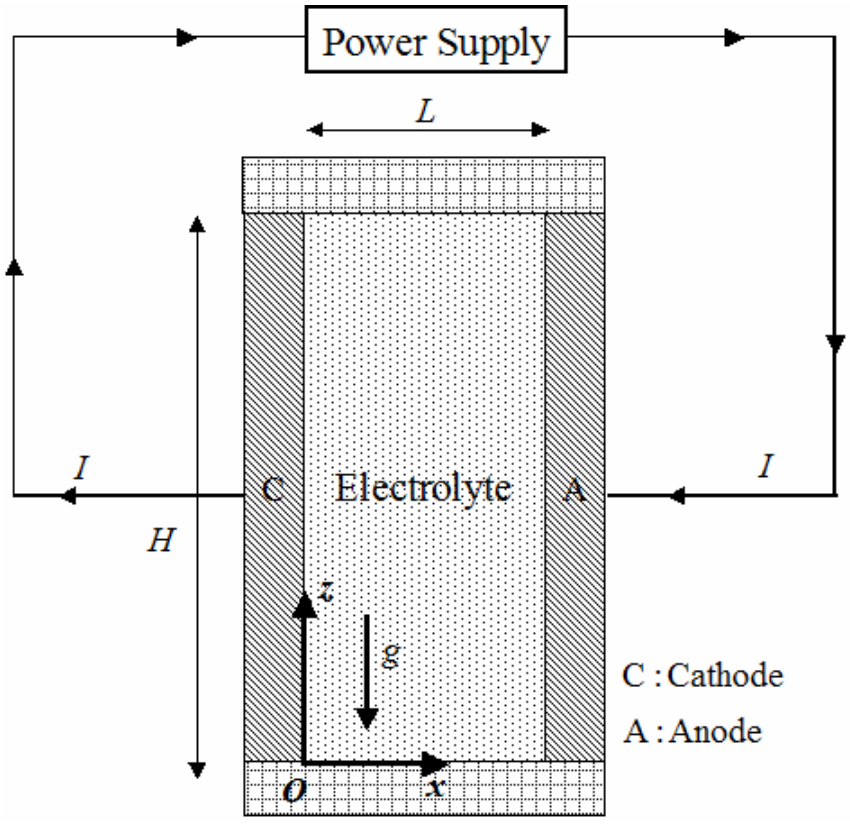

Figure 2.1: Schematic diagram of the 2D electrolytic cell.

The two vertical walls are the electrodes, and the bottom and top of container are the electrically insulated walls. The vertical electrode height is denoted by H and the electrode spacing L. Both electrodes are made of the same metallic material. The left (or right) electrode is the cathode (or anode) where the electrochemical deposition (or dissolution) of metal takes place on the surface. The electric current flow is generated by the power supply apparatus. The total electric current over the whole electrode surface area is denoted by I. The power supply is controlled to provide a constant total electric current.

The electrolyte is a dilute aqueous solution composed of a mixture of the small amount of a chemical compound and the excess amount of distilled water. A chemical compound is metallic salt composed of the same metallic ion species as electrode material. A mixture of the chemical compound and distilled water is called the fluid. Below given are the basic equations describing physicochemical hydrodynamic phenomena during the electrochemical reactions.

2.2 Model Equation

Mathematical model includes the unsteady advection-diffusion equation for the concentration of a chemical compound,

$$\frac{\mathrm{D}m}{\mathrm{D}t} = D\nabla^2 m. \tag{2-1}$$

Here, m is the concentration of a chemical compound, D the diffusion coefficient, and t the time. $\mathrm{D}/\mathrm{D}t$ stands for the substantial derivative. The continuity and Navier-Stokes equations for the incompressible viscous fluid motion are written as

$$\frac{\mathrm{D}\rho}{\mathrm{D}t} + \rho\nabla\cdot\boldsymbol{u} = 0, \tag{2-2}$$

$$\frac{\mathrm{D}\boldsymbol{u}}{\mathrm{D}t} = -\frac{1}{\rho}\nabla p + \nu\nabla^2\boldsymbol{u} + \boldsymbol{g}. \tag{2-3}$$

Here, ρ is the fluid density, $\boldsymbol{u}$ the fluid velocity, p the pressure, ν the kinematic viscosity, and $\boldsymbol{g}$ the gravitational acceleration.

When the additive amount of a chemical compound is very small, the linear relationship

$$\rho - \rho_0 = \rho_0\beta(m - m_0) \tag{2-4}$$

may be assumed between concentration and fluid density. Here, ρ_0 is the fluid density at the equilibrium concentration m=m_0, and β is the densification coefficient. A similar linear relationship is assumed between fluid temperature and density. The conversion of electric energy to thermal energy, the so called "Joule heating", takes place on the electrode/electrolyte interface due to the passage of an electrolytic current [29-a]. If a long-term charging is carried out at high electrolytic current, such a heat generation cannot be negligible. However, when the applied electrolytic current is sufficiently low, the variation of temperature can be negligible during the electrochemical reactions, as the temperature measurements with thermocouples usually made in the laboratory scale electrochemical system. Under the Bousinesq approximation, Eqs. (2-2) and (2-3) are transformed into

$$\nabla\cdot\boldsymbol{u} = 0, \tag{2-5}$$

$$\frac{\mathrm{D}\boldsymbol{u}}{\mathrm{D}t} = -\frac{1}{\rho_0}\nabla p + \nu\nabla^2\boldsymbol{u} + \beta(m - m_0)\boldsymbol{g}. \tag{2-6}$$

Here, the Bousinesq approximation implies that the fluid density is considered as a variable only in formulating the buoyancy term $\beta(m - m_0)\boldsymbol{g}$ and all other properties are taken as constant.

As the initial condition we assume that the concentration of a chemical compound is homogeneous and an aqueous solution is at rest before the onset of the electrochemical reactions, which may be written as

$$\begin{aligned} m &= m_0, \\ u &= 0, \\ w &= 0. \end{aligned} \tag{2-7}$$

Here, the variables (u, w) denote the (x, z) components of the fluid velocity. Just after completing the electrical circuit, the initial current density distribution on the electrode surface is considered as uniform in the vertical direction, that is,

$$j(z) = j_{\text{ave}} \quad (0 \le z \le H). \tag{2-8}$$

Here, j is the current density and j_{ave} is the average over the entire electrode surface. The current density means the electric current per unit electrode surface area.

No-slip boundary condition is applied on both the electrode and insulated wall surfaces, that is,

$$u(x, z) = w(x, z) = 0 \qquad \text{at } x=0,\ L \text{ and } z=0,\ H. \tag{2-9}$$

We describe below the boundary condition for the concentration of a chemical compound. Let us consider an electrolyte solution containing a 1:1 chemical compound AX. It completely dissociates into A^{z_1} and X^{z_2} ions in an aqueous solution based on the dissociation reaction,

$$\mathrm{AX} \rightarrow \mathrm{A}^{z_1} + \mathrm{X}^{z_2}. \tag{2-10}$$

Here, A^{z_1} and X^{z_2} represent the chemical formulas of cation and anion, respectively. z_1 and z_2 express the valencies of each ion, being positive for cation and negative for anion. When the concentration of a chemical compound AX is given by m and the concentrations of A^{z_1} and X^{z_2} ions are denoted as C_1 and C_2, we find

$$C_1 = C_2 = m. \tag{2-11}$$

These ion concentrations satisfy the electroneutrality condition,

$$\sum_{k=1}^{2} z_k C_k = 0. \tag{2-12}$$

This condition means that there exists the same number of equivalents of cations as anions, and solution is thus electrically neutral. Such an electroneutrality is observed in all regions except in thin electric double layer. Because the length scale of the double layer thickness is of the order of 10^{-9}-10^{-8} meters and the time scale is of the order of 10^{-9}-10^{-7} seconds, the electronutrality is a good approximation in order to describe physicochemical hydrodynamic phenomena over both the length scale of 10^{-3}-10^{0} meters and the time scale of 10^{0}-10^{4} seconds [29-b, 30-a].

We now describe the boundary condition for the concentration of a chemical compound on the electrode surface. It is based on the ionic mass transfer phenomena expressed by the dilute-solution theory [29-c]. That is, the flux density $\boldsymbol{N}_k$ of ion species k consists of diffusion, ionic migration, and advection terms,

$$\boldsymbol{N}_k = -D_k \nabla C_k - \mu_k C_k \nabla \phi + C_k \boldsymbol{u}. \tag{2-13}$$

Here, D_k and μ_k represent the diffusion coefficient and mobility of ion species k, and ϕ the electric potential. Note that μ_k has positive sign for cation and negative sign for anion, which means that cation and anoin move in the opposite direction with each other under an electric potential gradient.

Because no-slip boundary condition is applied on the electrode surface, the net mass flux of each ion species k normal to the electrode surface $N_{k,x}$ on the cathode (x=0) and anode (x=L) surfaces is given by

$$N_{k,x}\Big|_{x=0,L} = -D_k \left(\frac{\partial C_k}{\partial x} \right)\Bigg|_{x=0,L} - \mu_k \left(C_k \frac{\partial \phi}{\partial x} \right)\Bigg|_{x=0,L}. \tag{2-14}$$

After starting the electric current flow, the concentration boundary layers for both A^{z_1} and X^{z_2} ions inevitably develop due to the electrochemical reaction on the electrode/electrolyte interface and the condition of electroneutrality. Because the net mass flux of an ion species k produced by the electrochemical reaction $N_{k,x}$ on the electrode surface is expressed by Faraday's law [29-d], we find

$$N_{k,x}\Big|_{x=0,L} = -\frac{s_k}{nF} j. \tag{2-15}$$

Here, n is the number of electrons transferred in the electrochemical reaction, F the Faraday constant, and s_k is the stoichiometric coefficient for the generalized electrochemical reaction equation

$$\sum_k s_k \mathrm{M}_k^{z_k} \rightarrow ne^- \tag{2-16}$$

with M_k being the symbol of the chemical formula. Only the electrochemical deposition and dissolution of metal are considered as the electrochemical reactions on the electrode/electrolyte interface, and no other reactions take place. That is, only A^{z_1} ion reacts on the electrode/electrolyte interface. On the cathode surface, the electrochemical deposition of metal A takes place, which may be written as

$$\mathrm{A}^{z_1} + ne^- \rightarrow \mathrm{A}. \tag{2-17}$$

On the other hand, the reverse reaction of Eq. (2-17) takes place on the anode surface. The boundary conditions for A^{z_1} and X^{z_2} ions on the electrode surfaces are written as

$$N_{1,x}\Big|_{x=0,L} = -D_1 \frac{\partial C_1}{\partial x}\bigg|_{x=0,L} - \mu_1 \left(C_1 \frac{\partial \phi}{\partial x} \right)\bigg|_{x=0,L} = \frac{j}{nF}, \tag{2-18}$$

$$N_{2,x}\Big|_{x=0,L} = -D_2 \frac{\partial C_2}{\partial x}\bigg|_{x=0,L} - \mu_2 \left(C_2 \frac{\partial \phi}{\partial x} \right)\bigg|_{x=0,L} = 0. \tag{2-19}$$

Based on the condition of electroneutrality, we find

$$-\frac{-\mu_2 D_1+\mu_1 D_2}{-\mu_2+\mu_1}\left.\frac{\partial m}{\partial x}\right|_{x=0,L}=\left(1-\frac{\mu_1}{-\mu_2+\mu_1}\right)\frac{j}{nF}, \qquad (2\text{-}20)$$

under the presumption of constant physical properties. Then, we obtain

$$-D\left.\frac{\partial m}{\partial x}\right|_{x=0,L}=\frac{\left(1-{}^{*}t_1\right)}{nF}j. \qquad (2\text{-}21)$$

Here,

$$D=\frac{-\mu_2 D_1+\mu_1 D_2}{-\mu_2+\mu_1} \qquad (2\text{-}22)$$

is the diffusion coefficient of a chemical compound AX appearing in Eq. (2-1). It is expressed by combining the diffusivities of A^{z_1} and X^{z_2} ions with their mobilities. D is called the "binary electrolyte diffusion coefficient" [29-c]. Here,

$${}^{*}t_1=\frac{\mu_1}{-\mu_2+\mu_1} \qquad (2\text{-}23)$$

is the transference number of A^{z_1} ion in a binary AX aqueous electrolyte solution. It represents the mass flux of A^{z_1} ion transferred by the ionic migration term.

Boundary condition for the concentration on the electrically insulated bottom and top wall surfaces is based on the presumption that no electrochemical reaction takes place on these interfaces, that is,

$$\left.\frac{\partial m}{\partial z}\right|_{z=0,H}=0. \qquad (2\text{-}24)$$

2.3 Current Density Distribution

Now we describe the calculation procedure for local current density j along the electrode surface. Although the overall electric current I is constant, the local current density j is not uniform along the electrode surface but varies depending upon the

concentration of a reactant metallic ion at the corresponding position. Random thermal collisions of a reactant ion on the electrode/electrolyte interface cause the electrode reaction to take place, sometimes in the anodic direction and sometimes cathodic direction. At the equilibrium condition, the rate of the anodic reaction is equal to that of the cathodic reaction.

Figure 2.2 shows the schematic of the relative energy difference of the electron in anodic and cathodic reactions [29-e].

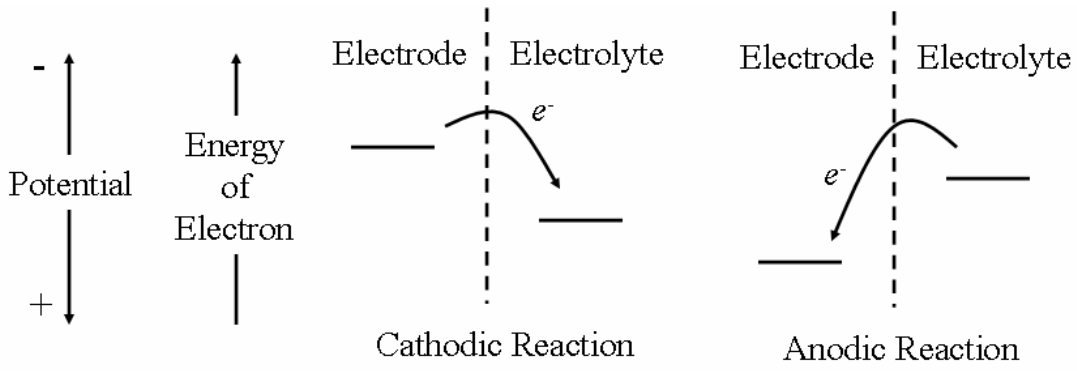

Figure 2.2: Schematic description of the relative energy difference of the electron in anodic and cathodic reactions. The dashed line indicates the electrode/electrolyte interface.

The driving force for electrode reaction is determined by the thermodynamic properties of the electrode and electrolyte solution. These thermodynamic properties are the electrochemical potentials. The electrochemical potential difference between the electrode and electrode/electrolyte interface is the driving force for electrode reaction. The rate of electrode reaction in response to this driving force depends on the kinetic rate parameter. Therefore, it is indispensable to express the effect of this potential difference on the rate of electrode reaction. During the anodic reaction, electrons are

transferred from the electrode to the lowest unoccupied energy level of a reactant species on the electrode/electrolyte interface. On the other hand, vice versa takes place during the cathodic reaction. Thus, applying a positive (or negative) potential relative to the equilibrium potential of electrode drives the reaction in the anodic (or cathodic) direction. The rate of electrode reaction is characterized by the current density as expressed by Eq. (2-15). The potential difference between the electrode and electrode/electrolyte interface is termed the "electrode surface overpotential", and it is given by the symbol η_S. The rate of electrode reaction is often related to η_S by the Butler-Volmer equation, which has the form

$$j = j_{e,0}\left(\frac{C_{1,S}}{C_{1,0}}\right)^{\gamma}\left(\exp\left[\frac{\alpha_A F}{RT}\eta_S\right] - \exp\left[-\frac{\alpha_C F}{RT}\eta_S\right]\right). \tag{2-25}$$

Here, R expresses the universal gas constant and T represents the temperature. The first term in the right hand of Eq. (2-25) is the rate of the anodic direction, while the second is that of the cathodic direction. The difference between these rates gives the net rate of electrode reaction. The parameter $j_{e,0}$ is called the exchange current density and is analogous to the rate constant used in chemical kinetics. The net direction of electrode reaction depends on the sign of j. The current density has negative value for the cathodic reaction and positive for the anodic reaction. The parameters α_A and α_C, called "apparent transfer coefficients", are additional kinetic parameters that relate how an applied potential difference favors one direction of electrode reaction over the other. The rate of electrode reaction depends on the concentration of a reactant ion species in the electrolyte solution adjacent to the electrode surface. It is just outside the electric double layer, because the double layer is regarded as the part of the electrode/electrolyte interface [29-f]. The parameter γ

expresses how the concentration of a reactant metallic ion species on the electrode surface influences the rate of electrode reaction. The numerical values of α_A, α_C, and γ generally depend on the nature of electrode reaction such as the process of electron transfer across the electrode/electrolyte interface.

In the right hand of Eq. (2-25), all symbols except for $C_{1,S}$ and η_S are constant. $C_{1,S}$ expresses the electrode surface concentration of A^{z_1} ion, and it is a variable to be computed in the numerical calculation. η_S is uniform along the vertical direction and it is numerically calculated by the constraint that the integration of local current density over the whole effective electrode surface area is equal to the constant overall electric current I, that is,

$$I = \int jdA = \int_0^H jdz = j_{\text{ave}} H. \tag{2-26}$$

Here, $A(=H)$ expresses the total electrode surface area per unit electrode depth. Therefore, η_S gives a measure of degree of nonequilibrium to drive an overall electric current I.

2.4 Dimensionless Expression

The governing equations (2-1), (2-5) and (2-6) are non-dimensionalized by introducing the following variables:

$$x' = x/x_0\,,\quad z' = z/x_0\,,\quad u' = u/u_0\,,\quad w' = w/u_0\,,\quad t' = t/(x_0/u_0),\quad p' = p/\rho_0 u_0^2\,,\quad m' = m/m_0\,. \tag{2-27}$$

Here, the variables with subscript 0 are reference scale values defined later. The non-dimensional governing equations read as

$$\frac{\partial m'}{\partial t'} + u'\frac{\partial m'}{\partial x'} + w'\frac{\partial m'}{\partial z'} = \frac{1}{\mathrm{Sc}\cdot\mathrm{Re}}\nabla'^2 m', \tag{2-28}$$

$$\frac{\partial u'}{\partial x'} + \frac{\partial w'}{\partial z'} = 0, \tag{2-29}$$

$$\frac{\partial u'}{\partial t'} + u'\frac{\partial u'}{\partial x'} + w'\frac{\partial u'}{\partial z'} = -\frac{\partial p'}{\partial x'} + \frac{1}{\mathrm{Re}}\nabla'^2 u', \tag{2-30}$$

$$\frac{\partial w'}{\partial t'} + u'\frac{\partial w'}{\partial x'} + w'\frac{\partial w'}{\partial z'} = -\frac{\partial p'}{\partial z'} + \frac{1}{\mathrm{Re}}\nabla'^2 w' - \frac{\mathrm{Gr}}{\mathrm{Re}^2}(m'-1). \tag{2-31}$$

Here,

$$\mathrm{Sc} = \frac{\nu}{D} \tag{2-32}$$

is the Schmidt number,

$$\mathrm{Re} = \frac{x_0 u_0}{\nu} \tag{2-33}$$

the Reynolds number, and

$$\mathrm{Gr} = \frac{x_0^3 m_0 \beta g}{\nu^2} \tag{2-34}$$

the Grashof number.

The reference scales are defined as follows. The electrode spacing L is chosen as the reference length scale x_0:

$$x_0 = L. \tag{2-35}$$

The reference velocity scale u_0 is determined as

$$u_0 = \frac{D}{H}\left(\mathrm{Sc}\cdot\mathrm{Gr}^*\big|_{z=H}\right)^{2/5}, \tag{2-36}$$

from the analytical solution of the laminar boundary layer equations for free convection along a vertical plane electrode having uniform current density j_{ave} [31-33] (see Appendix). Here,

$$\mathrm{Gr}^*\big|_{z=H} = \frac{g\beta(1-{}^*t_1)j_{\mathrm{ave}}H^4}{nFD\nu^2} = \frac{g\beta(1-{}^*t_1)j_{\mathrm{ave}}x_0^4 B^4}{nFD\nu^2} \tag{2-37}$$

is the modified Grashof number at z=H, and

$$B = \frac{H}{L} \tag{2-38}$$

is the aspect ratio. From the above estimation of reference scales, it is recognized that L, B, and j_{ave} are controlling factors to determine the dimensionless numbers.

2.5 Discretization Procedure

Using the first-order backward difference scheme for time discretization, we write the governing equations (2-28)-(2-31) as

$$\frac{m'^{N+1} - m'^{N}}{\Delta t'} + \left[u' \frac{\partial m'}{\partial x'} \right]^{N+1} + \left[w' \frac{\partial m'}{\partial z'} \right]^{N+1} = \frac{1}{\mathrm{Sc} \cdot \mathrm{Re}} \left[\nabla'^2 m' \right]^{N+1}, \tag{2-39}$$

$$\begin{aligned} \left[\nabla'^2 p' \right]^{N+1} = & -\left[\left(\frac{\partial u'^{N+1}}{\partial x'} \right)^2 + 2 \left(\frac{\partial w'^{N+1}}{\partial x'} \right) \left(\frac{\partial u'^{N+1}}{\partial z'} \right) + \left(\frac{\partial w'^{N+1}}{\partial z'} \right)^2 \right] \\ & - \frac{\left[\nabla' \cdot \boldsymbol{u}' \right]^{N+1} - \left[\nabla' \cdot \boldsymbol{u}' \right]^{N}}{\Delta t'} - \frac{\mathrm{Gr}}{\mathrm{Re}^2} \left(\frac{\partial m'^{N+1}}{\partial z'} \right), \end{aligned} \tag{2-40}$$

$$\frac{u'^{N+1} - u'^{N}}{\Delta t'} + \left[u' \frac{\partial u'}{\partial x'} \right]^{N+1} + \left[w' \frac{\partial u'}{\partial z'} \right]^{N+1} = -\left[\frac{\partial p'}{\partial x'} \right]^{N+1} + \frac{1}{\mathrm{Re}} \left[\nabla'^2 u' \right]^{N+1}, \tag{2-41}$$

$$\begin{aligned} \frac{w'^{N+1} - w'^{N}}{\Delta t'} + \left[u' \frac{\partial w'}{\partial x'} \right]^{N+1} + \left[w' \frac{\partial w'}{\partial z'} \right]^{N+1} = & -\left[\frac{\partial p'}{\partial z'} \right]^{N+1} + \frac{1}{\mathrm{Re}} \left[\nabla'^2 w' \right]^{N+1} \\ & + \frac{\mathrm{Gr}}{\mathrm{Re}^2} \left(1 - m'^{N+1} \right). \end{aligned} \tag{2-42}$$

Here, superscripts N and N+1 indicate the time steps. Given the numerical values at $t' = N \cdot \Delta t'$, those at $t' = (N+1) \cdot \Delta t'$ are computed. Eq. (2-40) is the Poisson equation for pressure, where p'^{N+1} is determined so as to make $\left[\nabla' \cdot \boldsymbol{u}' \right]^{N+1}$ zero.

The convective terms in Eqs. (2-39), (2-41) and (2-42) are approximated in a linear form for u'^{N+1} and w'^{N+1}, that is,

$$\left[u'\frac{\partial m'}{\partial x'}\right]^{N+1} \approx u'^{N}\left(\frac{\partial m'}{\partial x'}\right)^{N+1},$$

$$\left[w'\frac{\partial m'}{\partial z'}\right]^{N+1} \approx w'^{N}\left(\frac{\partial m'}{\partial z'}\right)^{N+1},$$

$$\left[u'\frac{\partial u'}{\partial x'}\right]^{N+1} \approx u'^{N}\left(\frac{\partial u'}{\partial x'}\right)^{N+1},$$

$$\left[w'\frac{\partial u'}{\partial z'}\right]^{N+1} \approx w'^{N}\left(\frac{\partial u'}{\partial z'}\right)^{N+1},$$

$$\left[u'\frac{\partial w'}{\partial x'}\right]^{N+1} \approx u'^{N}\left(\frac{\partial w'}{\partial x'}\right)^{N+1},$$

$$\left[w'\frac{\partial w'}{\partial z'}\right]^{N+1} \approx w'^{N}\left(\frac{\partial w'}{\partial z'}\right)^{N+1}.$$

The first term in the right hand of Eq. (2-40) is approximated by

$$\left[\left(\frac{\partial u'^{N+1}}{\partial x'}\right)^2 + 2\left(\frac{\partial w'^{N+1}}{\partial x'}\right)\left(\frac{\partial u'^{N+1}}{\partial z'}\right) + \left(\frac{\partial w'^{N+1}}{\partial z'}\right)^2\right]$$
$$\approx \left[\left(\frac{\partial u'^{N}}{\partial x'}\right)^2 + 2\left(\frac{\partial w'^{N}}{\partial x'}\right)\left(\frac{\partial u'^{N}}{\partial z'}\right) + \left(\frac{\partial w'^{N}}{\partial z'}\right)^2\right].$$

The computational grid with uneven interval mesh size in the x direction is employed in order to describe the thin concentration boundary layer formed along the electrode surface more accurately. The non-dimensional concentration boundary layer thickness may be estimated as $\delta' = (\mathrm{Sc}\cdot\mathrm{Re})^{-1/2}$ from the scaling analysis of Eq. (2-28). When the Schmidt number is 2740 and the Reynolds number is 0.5, corresponding to typical model case of the present numerical calculation, we have $\delta' = 2.7\times10^{-2}$. The uneven mesh size in the x direction is generated from the electrode surface to the middle line of the electrode spacing by a geometrical

progression as

$$
\begin{aligned}
&x'_1 = 0, \\
&x'_2 = \Delta x'_{\min}, \\
&x'_3 = x'_2 + \Delta x'_{\min} r, \\
&\vdots \\
&x'_M = x'_{M-1} + \Delta x'_{\min} r^{M-2}.
\end{aligned}
\tag{2-43}
$$

Here, subscript M indicates the grid number beginning with the electrode surface (M=1). Figure 2.3 shows the computational grid of 80×100 cells in the case of L [mm]=2 and H [cm]=1.

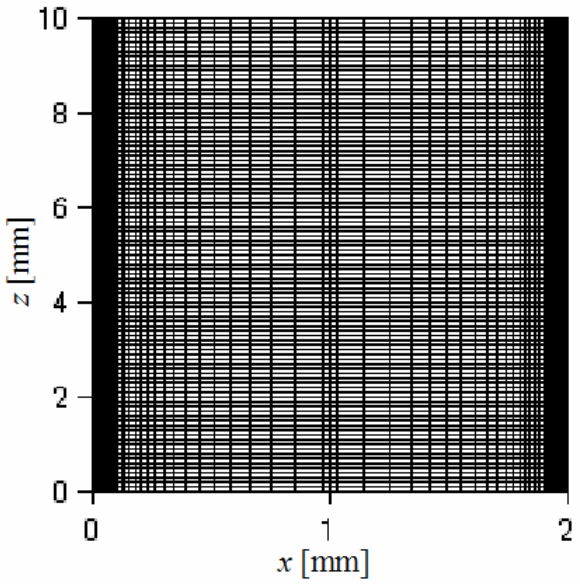

Figure 2.3: Computational grid of 80×100 cells employed in numerical simulation in the case of L [mm]=2 and H [cm]=1.

The minimal mesh length $\Delta x'_{\min}$ is set to 10^{-3} and the common ratio r less than 1.15 is employed in order not to make the numerical calculation extremely less accurate in the middle region of the electrode spacing. In the z direction, the mesh size is taken

uniform.

The non-dimensional physical 2D plane (x', z') is transformed to the calculation plane (ξ, ζ). Generally, the coordinate transformation is expressed by

$$\begin{aligned} x' &= x'(\xi, \zeta), \\ z' &= z'(\xi, \zeta). \end{aligned} \tag{2-44}$$

Then, the partial derivatives with respect to x' and z' are written as

$$\begin{aligned} \frac{\partial}{\partial x'} &= \frac{1}{J}\left(z'_{\zeta} \frac{\partial}{\partial \xi} - z'_{\xi} \frac{\partial}{\partial \zeta} \right), \\ \frac{\partial}{\partial z'} &= \frac{1}{J}\left(x'_{\xi} \frac{\partial}{\partial \zeta} - x'_{\zeta} \frac{\partial}{\partial \xi} \right). \end{aligned} \tag{2-45}$$

Here,

$$J = x'_{\xi}\, z'_{\zeta} - x'_{\zeta}\, z'_{\xi} \tag{2-46}$$

is the transform Jacobian. Here, subscripts ξ and ζ stand for the partial differentiation with respect to ξ and ζ, respectively. Then, Eqs. (2-39)-(2-42) are written as

$$\frac{m'^{N+1} - m'^{N}}{\Delta t'} + \frac{u'^{N} z'_{\xi} - w'^{N} x'_{\xi}}{J} m'^{N+1}_{\xi} + \frac{w'^{N} x'_{\xi} - u'^{N} z'_{\xi}}{J} m'^{N+1}_{\zeta} = \frac{1}{\mathrm{Sc} \cdot \mathrm{Re}} \nabla'^{2} m'^{N+1}, \tag{2-47}$$

$$\begin{aligned} \left[\nabla'^{2} p'\right]^{N+1} = &-\frac{1}{J^2}\left[\begin{array}{l} \left(z'_{\zeta} u'^{N}_{\xi} - z'_{\xi} u'^{N}_{\zeta} \right)^2 + 2\left(z'_{\xi} w'^{N}_{\xi} - z'_{\xi} w'^{N}_{\zeta} \right)\left(x'_{\xi} u'^{N}_{\zeta} - x'_{\zeta} u'^{N}_{\xi} \right) \\ + \left(x'_{\xi} w'^{N}_{\zeta} - x'_{\zeta} w'^{N}_{\xi} \right)^2 \end{array} \right] \\ &- \frac{1}{J\Delta t'}\left(z'_{\zeta} u'^{N}_{\xi} - z'_{\xi} u'^{N}_{\zeta} + x'_{\xi} w'^{N}_{\zeta} - x'_{\zeta} w'^{N}_{\xi} \right) - \frac{\mathrm{Gr}}{\mathrm{Re}^2} \frac{x'_{\xi} m'^{N+1}_{\zeta} - x'_{\zeta} m'^{N+1}_{\xi}}{J}, \end{aligned} \tag{2-48}$$

$$\begin{aligned} \frac{u'^{N+1} - u'^{N}}{\Delta t'} + \frac{u'^{N} z'_{\xi} - w'^{N} x'_{\xi}}{J} u'^{N+1}_{\xi} + \frac{w'^{N} x'_{\xi} - u'^{N} z'_{\xi}}{J} u'^{N+1}_{\zeta} = &-\frac{z'_{\zeta} p'^{N+1}_{\xi} - z'_{\xi} p'^{N+1}_{\zeta}}{J} \\ &+ \frac{1}{\mathrm{Re}}\left[\nabla'^{2} u'\right]^{N+1}, \end{aligned} \tag{2-49}$$

$$\begin{aligned} \frac{w'^{N+1} - w'^{N}}{\Delta t'} + \frac{u'^{N} z'_{\zeta} - w'^{N} x'_{\zeta}}{J} w'^{N+1}_{\xi} + \frac{w'^{N} x'_{\xi} - u'^{N} z'_{\xi}}{J} w'^{N+1}_{\zeta} = &-\frac{x'_{\xi} p'^{N+1}_{\zeta} - x'_{\zeta} p'^{N+1}_{\xi}}{J} \\ &+ \frac{1}{\mathrm{Re}}\left[\nabla'^{2} w'\right]^{N+1} + \frac{\mathrm{Gr}}{\mathrm{Re}^2}\left(1 - m'^{N+1}\right). \end{aligned} \tag{2-50}$$

The Laplace operator ∇'^{2} in the calculation plane is defined by

$$\nabla'^2 f = \frac{\alpha f_{\xi\xi} - 2\beta f_{\xi\zeta} + \gamma f_{\zeta\zeta}}{J^2} + \frac{\left(\alpha x'_{\xi\xi} - 2\beta x'_{\xi\zeta} + \gamma x'_{\zeta\zeta}\right)\left(z'_{\xi} f_{\zeta} - z'_{\zeta} f_{\xi}\right) + \left(\alpha z'_{\xi\xi} - 2\beta z'_{\xi\zeta} + \gamma z'_{\zeta\zeta}\right)\left(x'_{\zeta} f_{\xi} - x'_{\xi} f_{\zeta}\right)}{J^3}, \tag{2-51}$$

where

$$\begin{aligned} \alpha &= x'^2_{\zeta} + z'^2_{\zeta}, \\ \beta &= x'_{\xi} x'_{\zeta} + z'_{\xi} z'_{\zeta}, \\ \gamma &= x'^2_{\xi} + z'^2_{\xi}. \end{aligned} \tag{2-52}$$

For space discretization, the second-order central difference scheme

$$\begin{aligned} \left(\frac{\partial f}{\partial \xi}\right)_{(i,j)} &= \frac{f_{(i+1,j)} - f_{(i-1,j)}}{2\Delta\xi}, \\ \left(\frac{\partial f}{\partial \zeta}\right)_{(i,j)} &= \frac{f_{(i,j+1)} - f_{(i,j-1)}}{2\Delta\zeta}, \end{aligned} \tag{2-53}$$

is applied except for the convective term, for which the third-order upwind (Kawamura) difference scheme

$$\begin{aligned} f^N_{(i,j)}\left(\frac{\partial h}{\partial \xi}\right)^{N+1}_{(i,j)} = \frac{f^N_{(i,j)}}{12\Delta\xi}\left(-h^{N+1}_{(i+2,j)} + 8h^{N+1}_{(i+1,j)} - 8h^{N+1}_{(i-1,j)} + h^{N+1}_{(i-2,j)}\right) \\ + \frac{3\left|f^N_{(i,j)}\right|}{12\Delta\xi}\left(h^{N+1}_{(i+2,j)} - 4h^{N+1}_{(i+1,j)} + 6h^{N+1}_{(i,j)} - 4h^{N+1}_{(i-1,j)} + h^{N+1}_{(i-2,j)}\right), \end{aligned} \tag{2-54}$$

is adopted. Here, subscript (i, j) indicates the grid point in calculation plane (ξ, ζ).

A brief flow chart of numerical calculation at each time step is given as below.

(1) The concentration field $m'^{N+1}_{(i,j)}$ is calculated by solving Eq. (2-47) with boundary conditions. The concentration fields of each ion $C'^{N+1}_{1(i,j)}$ and

$C'^{N+1}_{2(i,j)}$ are calculated based on Eq. (2-11).

(2) Both anodic and cathodic current density distributions in the vertical direction are calculated by determining the electrode surface overpotential η_S based on Eqs. (2-25) and (2-26), in order to satisfy the constraint that the integration of local current density over the whole electrode surface area is equal to the applied constant overall electrolytic current *I*.

(3) The pressure field $p'^{N+1}_{(i,j)}$ is calculated by numerically solving Eq. (2-48) with boundary conditions.

(4) The velocity fields $u'^{N+1}_{(i,j)}$ and $w'^{N+1}_{(i,j)}$ are numerically calculated by solving Eqs. (2-49) and (2-50) with boundary conditions.

In all numerical calculations, $\Delta t' = 10^{-4}$ is employed. The iterative calculation procedure for concentration, current density distribution, pressure, and velocity fields is based on the Successive Over-Relaxation (S.O.R) method. The iteration is finished when the absolute values of difference between the successive iteration counts, i.e. $\left|m'^{(I)}_{(i,j)} - m'^{(I-1)}_{(i,j)}\right|$, $\left|p'^{(I)}_{(i,j)} - p'^{(I-1)}_{(i,j)}\right|$, $\left|u'^{(I)}_{(i,j)} - u'^{(I-1)}_{(i,j)}\right|$, and $\left|w'^{(I)}_{(i,j)} - w'^{(I-1)}_{(i,j)}\right|$ are less than 10^{-2} respectively, and $\left|j_{\text{ave}}{}^{(I)} - j_{\text{ave}}{}^{(I-1)}\right|$ is less than 10^{-4}. Here, superscripts in parenthesis (*I*) and (*I*-1) express the number of iterations.

Appendix Laminar Boundary Layer Equations for Free Convection along a Vertical Electrode with Uniform Current Density

We consider the steady boundary layer flow formed along the vertical plane electrode in the coordinate system as shown in Figure A.1.

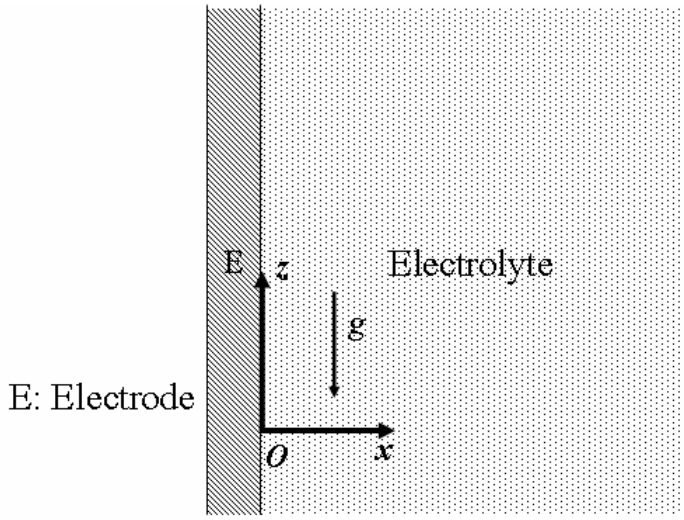

Figure A.1: Coordinate system to be considered.

The infinitely-long vertical plane electrode is immersed in an aqueous electrolyte solution. It is assumed that the electrode spacing is large enough to neglect the effect caused by the counter electrode. From the scaling analysis, we neglect the pressure gradient and viscous dissipation with respect to the z direction in Eqs. (2-1), (2-5), and (2-6). The governing equations expressing the conservations of mass, momentum, and concentration for laminar free convection in the boundary layer are written as

$$u\frac{\partial m}{\partial x}+w\frac{\partial m}{\partial z}=D\frac{\partial^2 m}{\partial x^2}, \tag{A-1}$$

$$\frac{\partial u}{\partial x}+\frac{\partial w}{\partial z}=0, \tag{A-2}$$

$$u\frac{\partial w}{\partial x}+w\frac{\partial w}{\partial z}=\nu\frac{\partial^2 w}{\partial x^2}-g\beta\left(m-m_0\right). \tag{A-3}$$

The solution of Eq. (A-2) is written in terms of the streamfunction ψ defined by

$$u=\frac{\partial\psi}{\partial z}, w=-\frac{\partial\psi}{\partial x}. \tag{A-4}$$

By introducing similarity variables,

$$\eta=E_1 z^{-1/5}x, \tag{A-5}$$

$$F\left(\eta\right)=\frac{\psi z^{-4/5}}{E_2}, \tag{A-6}$$

$$H\left(\eta\right)=\frac{E_1 nFD\left(m-m_0\right)}{\left(1-{}^{*}t_1\right)j_{\mathrm{ave}}z^{1/5}}, \tag{A-7}$$

the partial differential equations (A-1) and (A-3) are transformed to ordinary differential equations. Here, the numerical values of E_1 and E_2 are defined by

$$E_1=\left(\frac{g\beta\left(1-{}^{*}t_1\right)j_{\mathrm{ave}}\mathrm{Sc}}{nFD\nu^2}\right)^{1/5}, \tag{A-8}$$

$$E_2=DE_1=D\left(\frac{g\beta\left(1-{}^{*}t_1\right)j_{\mathrm{ave}}\mathrm{Sc}}{nFD\nu^2}\right)^{1/5}. \tag{A-9}$$

The vertical velocity component w is written as

$$w=DE_1^2 z^{3/5}\left(\frac{dF}{d\eta}\right)=\left(\mathrm{Sc}\cdot\mathrm{Gr}^{*}\right)^{2/5}\frac{D}{z}\left(\frac{dF}{d\eta}\right). \tag{A-10}$$

Then, we obtain

$$\left(\frac{d^2H}{d\eta^2}\right)+\frac{4}{5}F\left(\frac{dH}{d\eta}\right)-\frac{1}{5}H\left(\frac{dF}{d\eta}\right)=0, \tag{A-11}$$

$$\left(\frac{d^3F}{d\eta^3}\right)+\frac{4}{5\mathrm{Sc}}F\left(\frac{d^2F}{d\eta^2}\right)-\frac{3}{5\mathrm{Sc}}\left(\frac{dF}{d\eta}\right)^2-H=0. \tag{A-12}$$

The boundary conditions are derived by noting that u=w=0 and

$$-D\left.\frac{\partial m}{\partial x}\right|_{x=0}=\frac{\left(1-{}^{*}t_1\right)}{nF}j_{\mathrm{ave}} \tag{A-13}$$

on the electrode surface $(x = 0)$, and that w=0 and $m = m_0$ at a great distance from the electrode surface $(x = \infty)$. By the use of Eqs. (A-6), (A-7), and (A-10), the boundary conditions are written as

$$F|_{\eta=0} = \left(\frac{dF}{d\eta}\right)\Big|_{\eta=0} = 0, \qquad \left(\frac{dH}{d\eta}\right)\Big|_{\eta=0} = -1, \tag{A-14}$$

$$\left(\frac{dF}{d\eta}\right)\Big|_{\eta\to\infty} = H|_{\eta\to\infty} = 0. \tag{A-15}$$

The numerical solution to the ordinary differential equations (A-11) and (A-12) subject to the boundary conditions (A-14) and (A-15) is obtained by a shooting method. Calculated result is obtained for the Schmidt number of 1000, which is the same order in the conventional electrochemical system.

Figure A.2 shows the numerical solution of $(dF/d\eta)$.

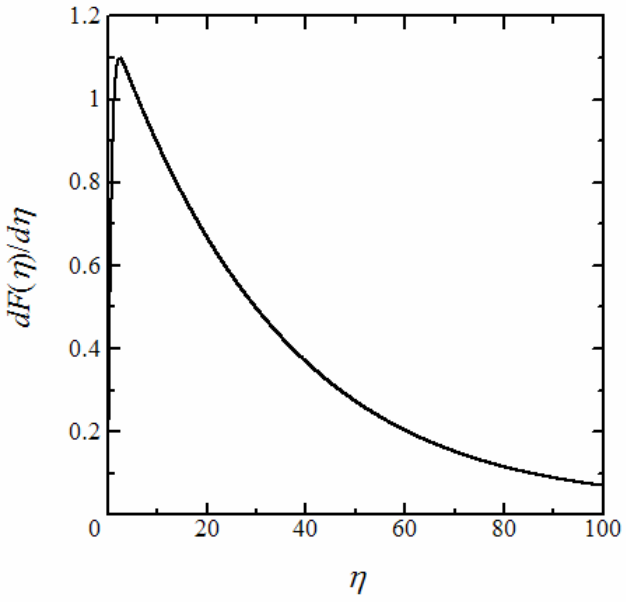

Figure A.2: Calculated result of $(dF/d\eta)$ at $\mathrm{Sc} = 1000$.

It is seen that the maximum value of $\left(dF/d\eta\right)$ becomes 1.1. Based on Eq. (A-10), the maximal vertical velocity component $w_{\max}$ is written as

$$w_{\max} = 1.1\frac{D}{z}\left(\mathrm{Sc}\cdot\mathrm{Gr}^{*}\right)^{2/5}. \tag{A-16}$$

We employ the value close to $w_{\max}$ at $z=H$ as the reference velocity, as shown in Eq. (2-36).

Section 3 Numerical Simulation in Copper Electrolysis System

3.1 Parameters in Electrochemical Model System

In this section, numerical simulation is carried out by the mathematical model developed in Section 2. Copper electrolysis in a binary copper sulfate ($CuSO_4$) aqueous solution is chosen as the model electrochemical system. It is because many studies have been carried out so far on mass transfer and physical property measurements during copper electrolysis in a $CuSO_4$ aqueous solution [16-23, 34-45]. The reproducibility of physicochemical phenomena accompanying the electrochemical reactions has been confirmed. The reaction mechanism of the electrochemical deposition and dissolution of copper is relatively simple, and a smooth copper film is electrochemically deposited as long as it is not too thick. Thus, copper electrolysis in a $CuSO_4$ aqueous solution is a good subject for the initial model numerical experiment.

In the case of copper electrolysis in a binary $CuSO_4$ aqueous solution, the cupric ion (Cu^{2+} ion) and the sulfuric acid ion (SO_4^{2-} ion) are present in liquid phase due to the dissociation reaction written as

$$CuSO_4 \rightarrow Cu^{2+} + SO_4^{2-}. \tag{3-1}$$

On the cathode/electrolyte interface, the electrochemical deposition of copper,

$$Cu^{2+} + 2e^{-} \rightarrow Cu, \tag{3-2}$$

takes place. The reverse reaction of Eq. (3-2) takes place on the anode/electrolyte interface. Referring to Section 2, Cu^{2+} ion is the cation and labeled 1 in symbols, and SO_4^{2-} ion is the anion and labeled 2. The number of electrons transferred in the electrochemical reaction is -2 for the cathodic reaction and +2 for the anodic reaction

based on Eq. (2-16). The physical properties of a binary $CuSO_4$ aqueous solution are listed in Table 3.1, which is based on the physical properties of a 0.6 M(=mol/dm^3) $CuSO_4$ aqueous solution [38-40]. The parameters associated with the electrochemical copper deposition and dissolution reactions are tabulated in this table [43-45].

Electrolyte Composition	0.6 M $CuSO_4$
D [m^2/s]	4.42×10^{-10}
ν [m^2/s]	1.21×10^{-6}
ρ_0 [kg/m^3]	1.09×10^{3}
β [m^3/mol]	1.4×10^{-4}
$^*t_1$ [-]	0.29
γ [-]	0.75
α_A [-]	1.5
α_C [-]	0.5
$j_{e,0}$ [mA/cm^2]	23.2

Table 3.1: Physical properties used in numerical simulation.

Table 3.2 lists the electrolytic conditions such as the predetermined electrolyte concentration of $CuSO_4$, the copper electrode height H, the electrode spacing L, the applied average current density j_{ave}, and the absolute temperature T. The electrode height is fixed value of 1 cm, and the electrode spacing is 1 or 2 mm.

Electrolyte Composition	0.6 M $CuSO_4$
Electrode Height H [cm]	1
Electrode Spacing L [mm]	1, 2
Applied Average Current Density j_{ave} [mA/cm^2]	1, 2
Temperature T [K]	298

Table 3.2: Electrolytic conditions.

Tables 3.3 summarizes the dimensionless numbers associating with the applied average current density j_{ave}, the aspect ratio B, the characteristic length scale x_0, and velocity scale u_0.

	j_{ave} [mA/cm^2]=1, L [mm]=2	j_{ave} [mA/cm^2]=2, L [mm]=1	j_{ave} [mA/cm^2]=2, L [mm]=2
Aspect Ratio $B(=H/L)$ [-]	5	10	5
Length Scale x_0 [m]	2.0×10^{-3}	1.0×10^{-3}	2.0×10^{-3}
Velocity Scale u_0 [m/s]	2.38×10^{-4}	3.15×10^{-4}	3.15×10^{-4}
Re [-]	3.94×10^{-1}	2.6×10^{-1}	5.2×10^{-1}
Sc [-]	2.74×10^{3}	2.74×10^{3}	2.74×10^{3}
Gr [-]	4.5×10^{3}	5.6×10^{2}	4.5×10^{3}

Table 3.3: Dimensionless numbers and reference scales.

3.2 Flow and Boundary Layer Structures

3.2.1 Velocity Field

We describe here the development mechanism of free convection. Figure 3.1 shows the contour of streamfunction Ψ (see Eq. (A-4) for definition) at various times after starting the electrochemical reactions in the case of (j_{ave} [mA/cm^2], L [mm])=(2, 2). The cathode is placed on the left side and the anode on the right side in all the subsequent figures. Note that the vertical size is reduced in this figure.

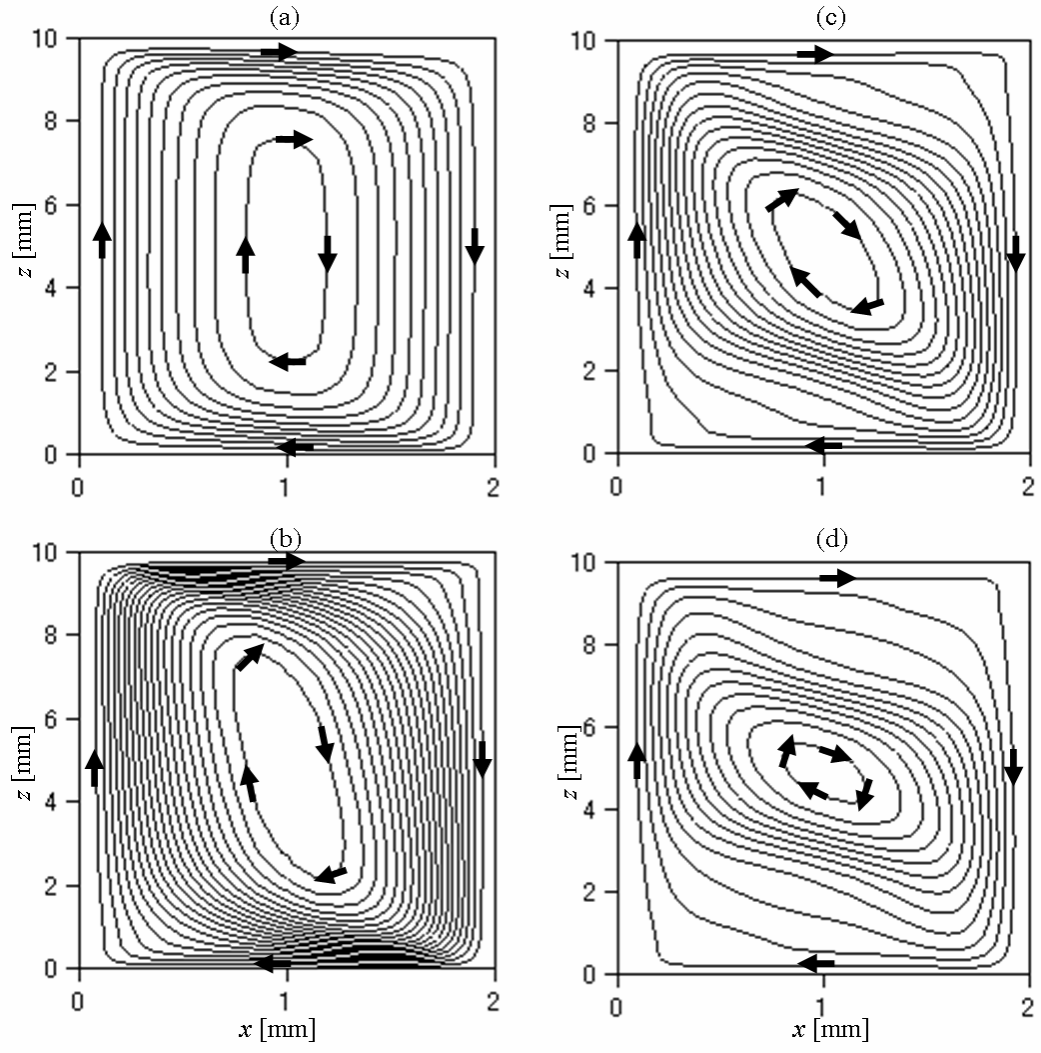

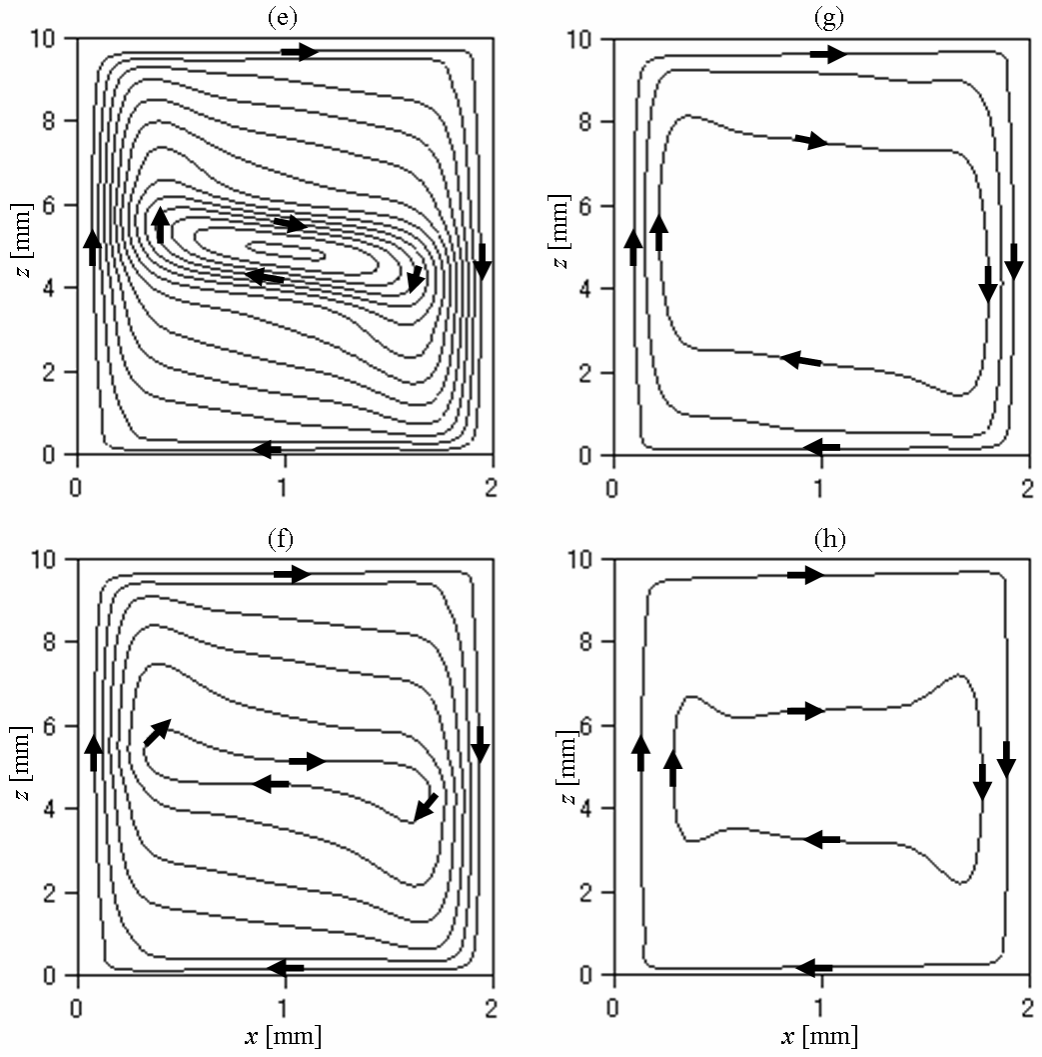

Figure 3.1: Time evolution of streamfunction $\Psi/u_0 x_0$. (a) t [s]=24, (b) 54, (c) 96, (d) 132, (e) 258, (f) 414, (g) 906, (h) 6000. The contour interval is $1/100$ in (a)-(d) and $1/200$ in (e)-(h). The flow direction is indicated by arrows.

The electrochemical reaction causes concentration difference near the electrode surface: a lighter (or heavier) electrolyte solution is produced near the cathode (or anode) surface. This induces the upward and downward convections along the vertical cathode and anode surfaces, respectively. They form a single swirling fluid motion compatible with this buoyant flow (Figure 3.1(a)). At the same time, the shear flows are formed along the top and bottom walls. These shear flows then get stronger. Figure 3.1(b) shows that the vortex starts to tilt and deform. The successive deformation process of this vortex structure (Figures 3.1(c)-(e)) is observed with decreasing intensity by viscous diffusion effects. Thereafter, the flow activity becomes further weaker except the vicinity of the cathode and anode surfaces where the upward and downward flows are continuously driven by buoyancy (Figures 3.1(f)-(h)). In Figure 3.1(h), the interior region is almost stagnant, whereas a boundary layer flow exists along the electrode and wall surfaces of the container.

Next, we examine the detailed flow structure by plotting a cross-sectional velocity profile. Figure 3.2 shows a typical time evolution of free convective velocity profile at the middle of the electrode height (z [mm]=5). The positive value of w indicates the upward flow, the negative one the downward flow. The velocity profile changes similarly in time. The velocity magnitude increases from zero on the electrode surface to a maximum, then gradually decreases toward the center line ($x=L/2$). The region between the electrode surface and the point that the velocity magnitude decreases to zero may be defined as the hydrodynamic boundary layer (HBL). As shown with the dotted and dashed lines, the HBL thickness is initially equal to $L/2$, and the maximal value of free convective velocity w_{max} in the HBL increases with time. It is consistent with the initial development of a single swirling fluid motion as seen in

Figures 3.1(a) and (b). Thereafter, the dashed-dot, dashed-two dotted and solid lines indicate that both the HBL thickness and w_{max} decrease with time due to the viscous effect. The dashed-two dotted and solid lines show that the interior region has almost no vertical component of the fluid velocity. At 6000 seconds, the solid line indicates that the HBL thickness and w_{max} decrease to about 0.4 mm and 0.04 mm/s, respectively.

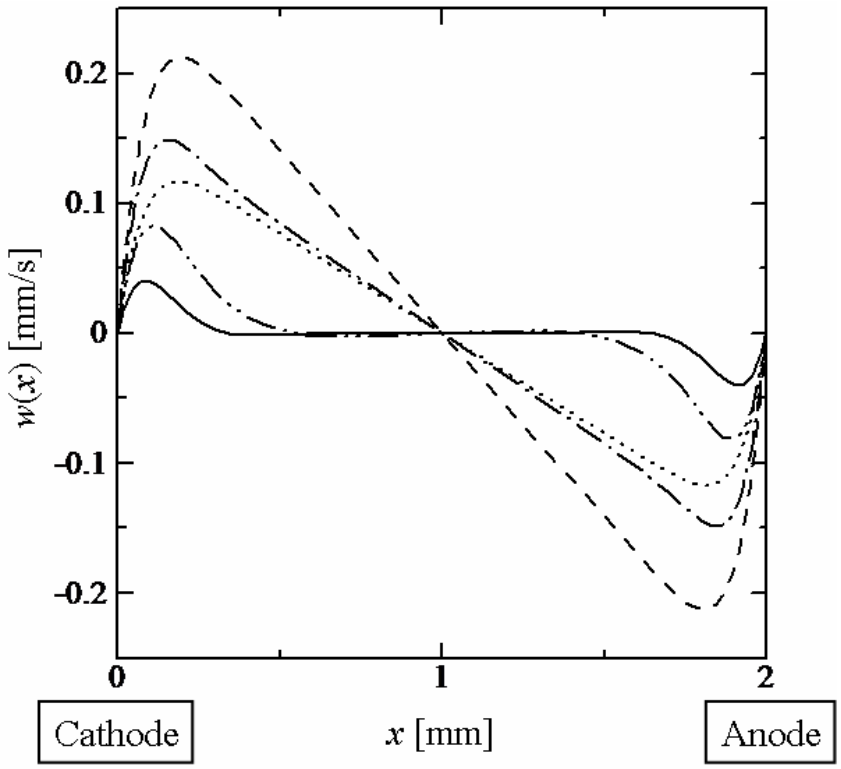

Figure 3.2: Transient variations in free convective velocity profile at z [mm]=5. The dotted line: t [s]=24, the dashed line: 54, the dashed-dotted line: 132, the dashed-two dotted line: 414, and the solid line: 6000.

Now, we examine the decay process of free convection quantitatively by looking at the time evolution of w_{max}.

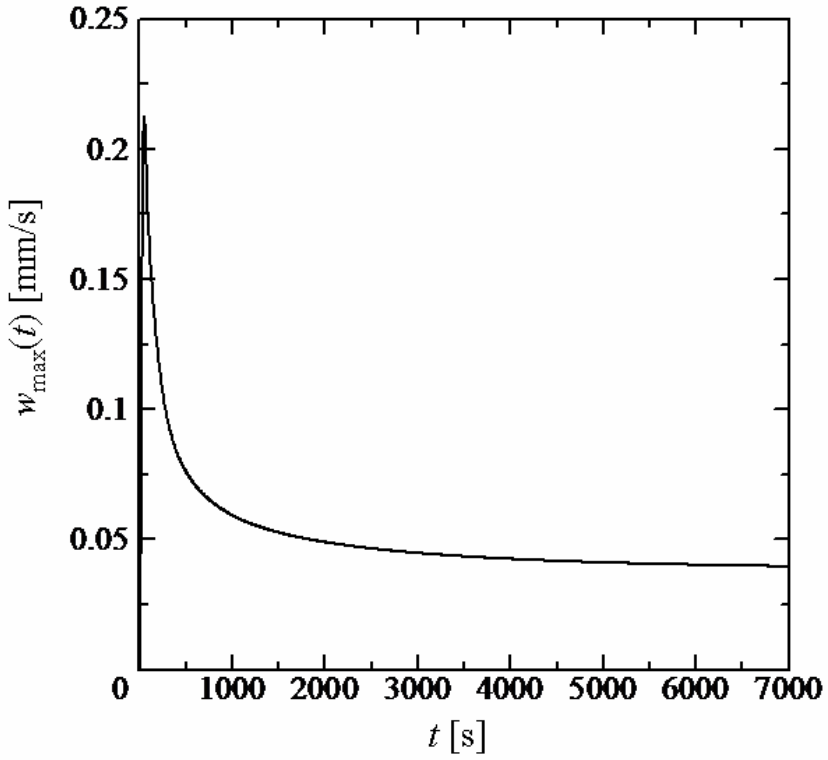

Figure 3.3: Time evolution of maximal free convective velocity w_{max} at z [mm]=5.

As seen in Figure 3.3, initially w_{max} increases rapidly and attains a maximum of 0.21 mm/s at t [s]=54. After that, it decreases first rapidly then slowly. Finally, it converges to about 0.04 mm/s as the time increases toward infinity. The decreasing region of w_{max} is compatible with the deformation and the subsequent weakening of the swirling flow by viscous diffusion effect in Figures 3.1(c)-(h).

Whether a steady state is attained or not may be examined more accurately by using the Shanks transformation. Let us denote the value of w_{max} at time t_n by $w(t_n)$,

and assume that as $t_n \to \infty$, $w_{\max}$ approaches a limit w_∞ as

$$w(t_n) = w_\infty + \alpha q^n, \tag{3-3}$$

where α and q are constants. Then, the ratio, the so called Shanks transformation,

$$A_n = \frac{w(t_{n+1})w(t_{n-1}) - w(t_n)^2}{w(t_{n+1}) + w(t_{n-1}) - 2w(t_n)} \tag{3-4}$$

may converge to w_∞ as the time increases more rapidly than $w(t_n)$. Figure 3.4 shows the time evolution of A_n thus calculated.

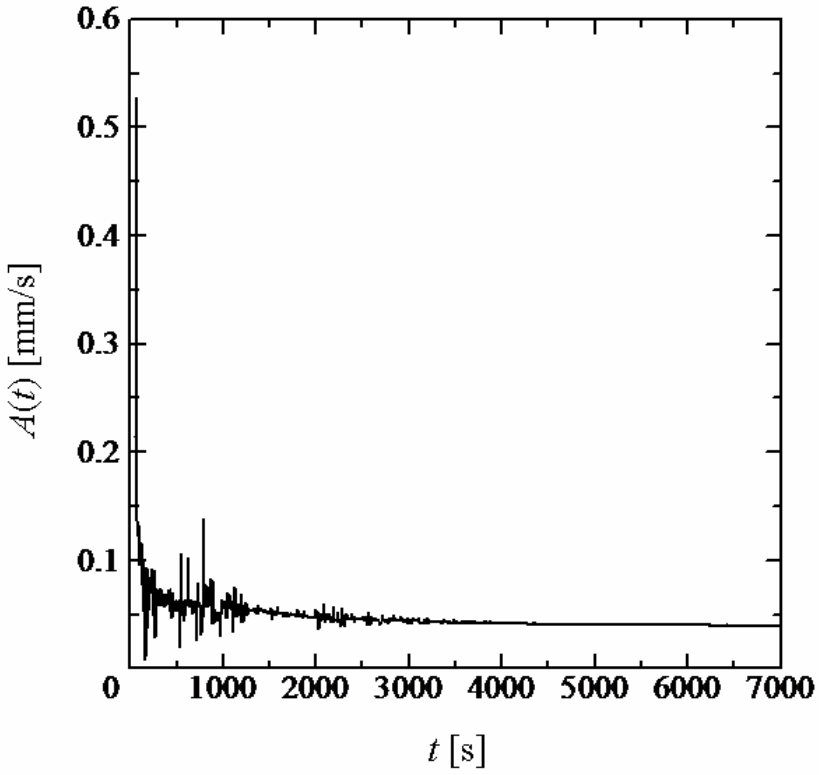

Figure 3.4: Time evolution of calculated $A(t)$ at z [mm]=5.

It is clearly seen that $A(t) \equiv A_n$ converges to a finite value of about 0.04 mm/s as the time increases after 3000 seconds. This value agrees well with $w_\infty = 0.04$ mm/s estimated from Figure 3.3. Therefore, we confirm that the present numerical calculation in the case of (j_{ave} [mA/cm^2], L [mm])=(2, 2) attains a steady state. We define in this study that the steady state is attained when w_{max} agrees with w_∞ estimated from the Schanks transformation with an accuracy of 1%. In the case of (2, 2), the steady state is attained at t [s]=6000.

As seen in Figure 3.1(h), the swirling flow at the steady state is confined to the vicinity of the electrode and wall surfaces. In order to capture the flow characteristics, we plot in Figure 3.5 the horizontal component of the fluid velocity on line x [mm]=1 and the vertical component on line z [mm]=5 at t [s]=6000. We observe clearly the HBL along the walls in which the fluid flows clockwise. The thickness of the vertical boundary layers is about 0.4 mm and the maximum value of velocity is about 0.04 mm/s. The flow fluxes in the upward and downward boundary layers are the almost same value of 6.3×10^{-3} mm^2/s per unit depth. As for the boundary layers along the top and bottom walls, the thickness is about 1 mm, the maximum value of velocity is about 0.015 mm/s, and the flow flux is estimated as 6.0×10^{-3} mm^2/s per unit depth. Therefore the flux is conserved in the boundary layers formed along the electrode, bottom, and top wall surfaces.

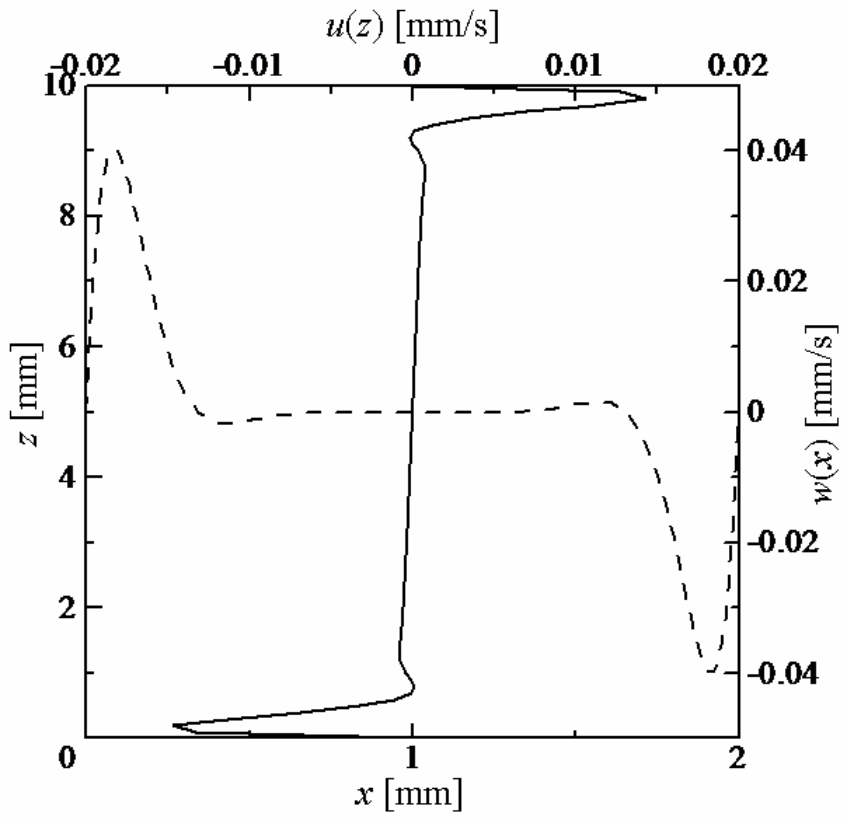

Figure 3.5: Velocity profiles at the steady state. The solid line: $u(z)$ on line x [mm]=1, the dashed line: $w(x)$ on line z [mm]=5. t [s]=6000.

3.2.2 Concentration Field

Figure 3.6 shows the contour of concentration profile at various times after the initiation of the electrochemical reactions in the case of (j_{ave} [mA/cm^2], L [mm])=(2, 2).

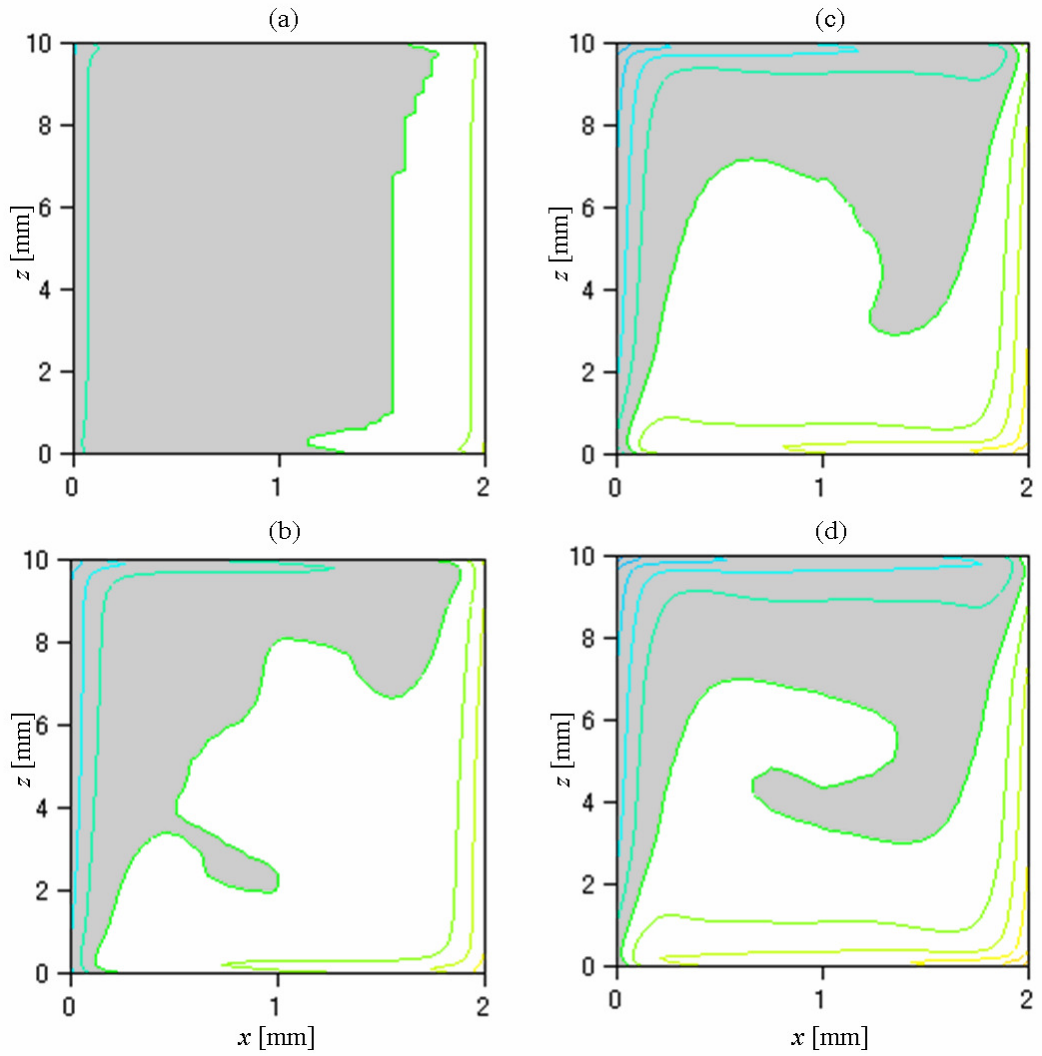
(a)
(c)
(b)
(d)
z [mm]
x [mm]
0
1
2
0
2
4
6
8
10

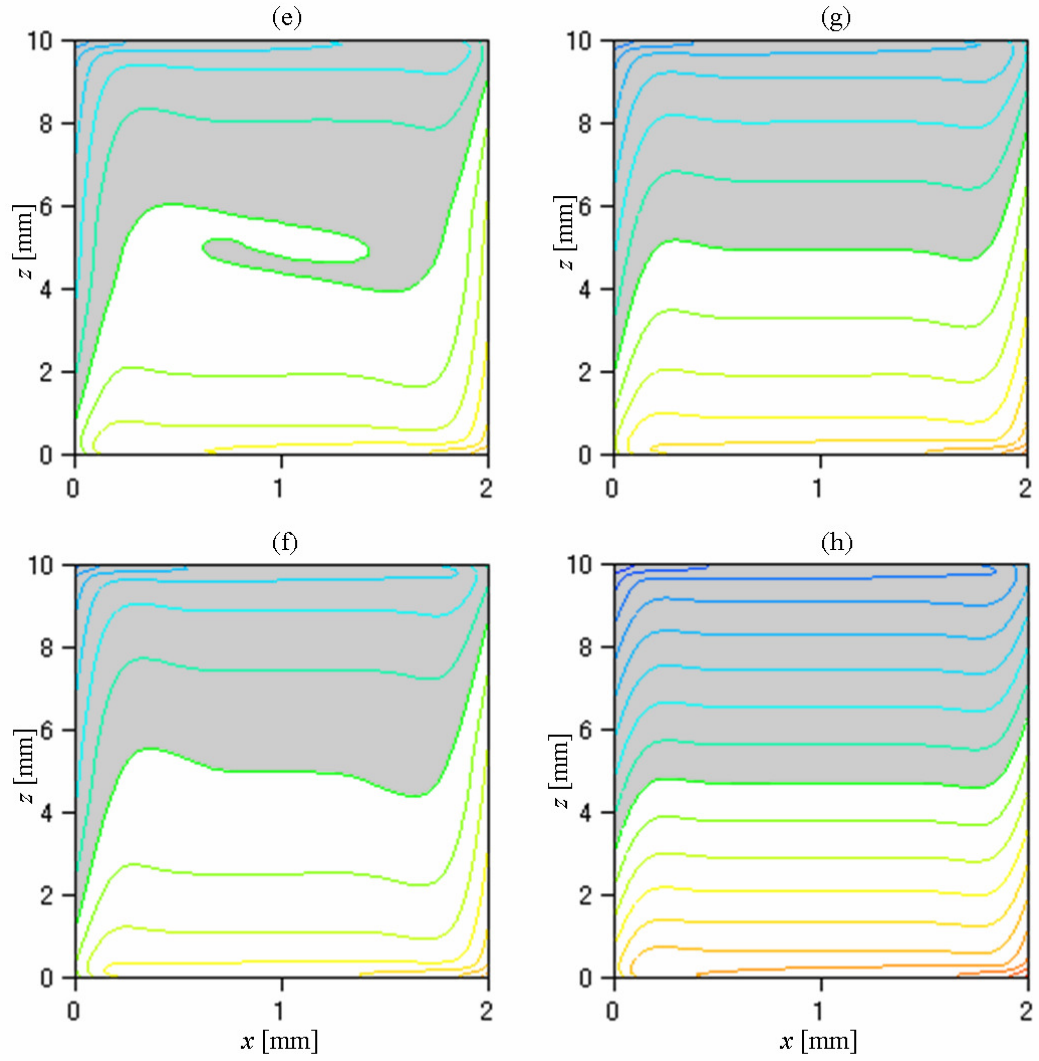

Figure 3.6: Transient variations in contour of concentration profile. (a) t [s]=24, (b) 54, (c) 96, (d) 132, (e) 258, (f) 414, (g) 906, (h) 6000. The region where the concentration is less than the initial value of 0.6 M is shaded. The contour interval is $m_0/30$.

Because the concentration of $CuSO_4$ is depleted (or enriched) near the cathode (or anode) surface due to the electrochemical deposition (or dissolution) of copper there, the concentration boundary layers (CBLs) are formed along the cathode and anode surfaces, respectively. At early times a swirling fluid motion is weak, so that the diffusion term dominates the advection term in the advection-diffusion equation. As seen in Eq. (2-21), the direction of mass flux caused by the electrochemical reaction is perpendicular to the electrode surface. The diffusion term mainly acts in the x direction near the electrode surface, so that the CBL thickness is almost uniform in the z direction (Figure 3.6(a)). Thereafter, the anodic and cathodic CBLs develop faster in the upper and lower end regions of $0<z<1$ and $9<z<10$, respectively (Figure 3.6(b)). As a swirling fluid motion develops, mass transport by the right- (or left-) ward flow near the top (or bottom) wall surface cannot be negligible. At the time of Figure 3.6(c), the supply of concentration from one electrode reaches the other electrode side by the rotational flow. In Figures 3.6(c)-(e), we observe the mass transfer by the swirling fluid motion. In the mean time, the stable electrolyte stratification is formed (Figures 3.6(g) and (h)) as the fluid motion gradually reduces to a steady swirling flow by viscous diffusion effects (Figures 3.1(g) and (h)). In Figures 3.6(f)-(h), the molecular diffusion in the z direction is seen. At the steady state, Figure 3.6(h) shows that the CBL thickness is almost uniform in the x direction except for the vicinity of the cathode and anode surfaces.

The steady state concentration profiles at z [mm]=1, 5, 9 are drawn in Figure 3.7. The CBL thickness has the almost same value of 0.17 mm in the both electrode sides. Referring to Section 2 (Page 17), the non-dimensional CBL thickness $\delta' = (\mathrm{Sc} \cdot \mathrm{Re})^{-1/2}$ may be estimated from the scaling analysis of Eq. (2-28). When

$w_\infty = 0.04$ mm/s is employed as the velocity scale, we have $\delta_\infty = x_0 (\mathrm{Sc} \cdot \mathrm{Re})^{-1/2} = 0.15$ mm, which is indicated with the dashed line in the figure. It agrees well with that estimated from the present numerical calculation.

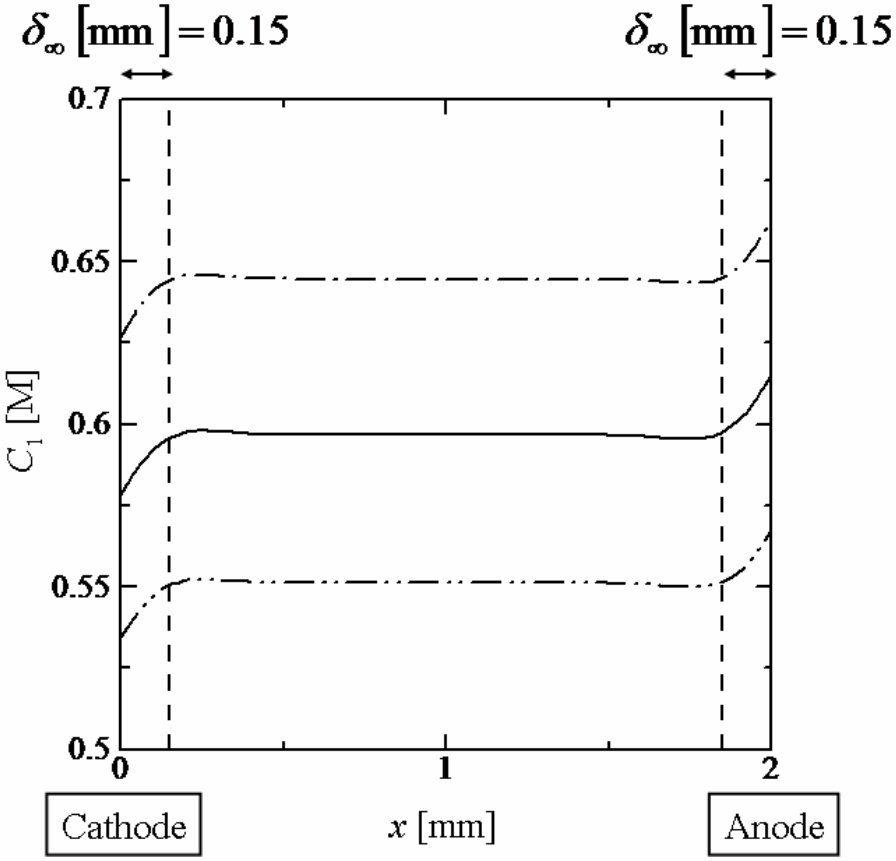

Figure 3.7: Steady state concentration profile of Cu^{2+} ion. The dashed-dotted line: z [mm]=1, the solid line: 5, and the dashed-two dotted line: 9. t [s]=6000.

The developments of vertical concentration distribution of Cu^{2+} ion and the current density distribution on the cathode surface (x [mm]=0) are plotted in Figure 3.8(a) and (b), respectively.

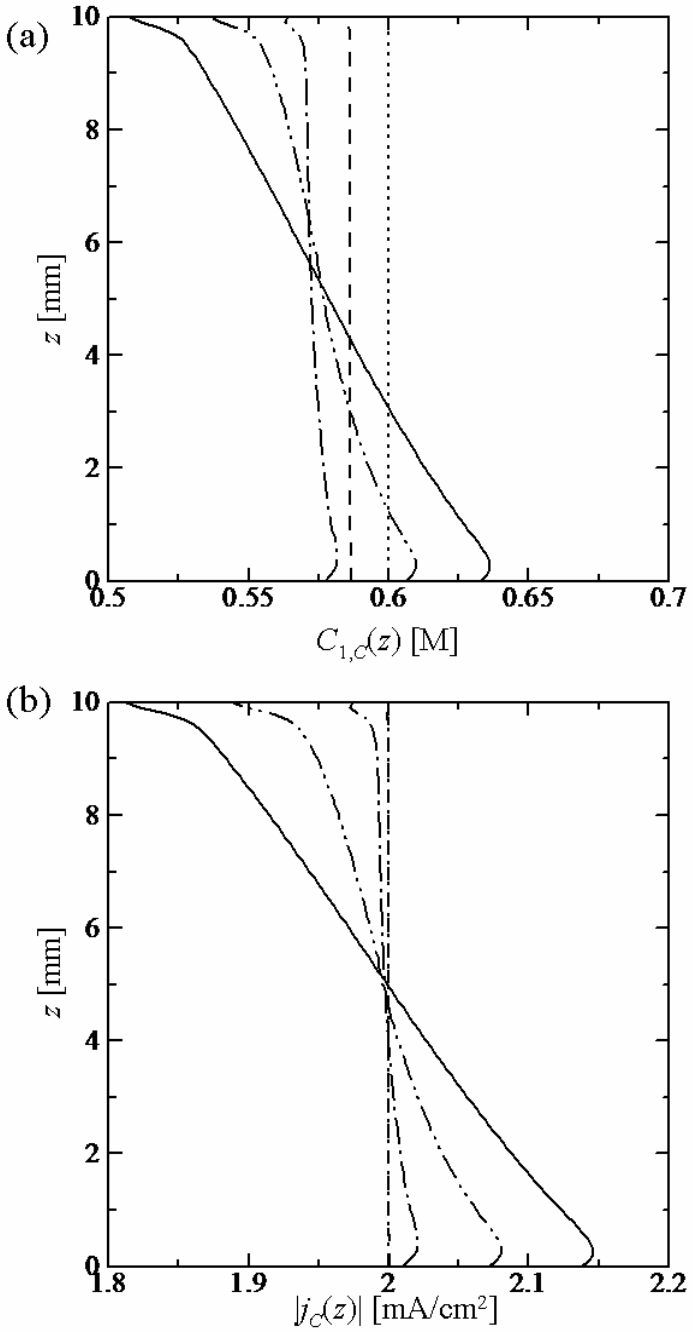

Figure 3.8: Vertical distribution of (a) concentration of Cu^{2+} ion and (b) current density on the cathode surface. The dotted line: t [s]=0, the dashed line: 10, the dashed-dotted line: 54, the dashed-two dotted line: 414, and the solid line: 6000. In (b), the lines at t=0 and 10 overlap each other.

The dashed line in these figures shows the almost vertically uniform distribution. In Figure 3.8(b), the dotted and dashed lines overlap each other, which implies that the vertical current density distribution remains unchanged during the initial 10 seconds. By the time t [s]=54, a heavier electrolyte solution produced near the anode surface is transferred to the cathode side by the rotational flow, and we observe an extreme value around z [mm]=0.5 in both the concentration and the current density distributions. This position is close to the maximum velocity point in the boundary layer along the bottom wall surfaces (see Figure 3.5).

3.3 Dependence of Nonuniformity of Current Density Distribution on Electrolytic Conditions

We investigate the effect of the operational conditions on the magnitude and decay behavior of convection. The time evolution of w_{max} in the HBL formed in the vicinity of the cathode surface at z [mm]=5 is employed as the typical barometer to describe transitional regime. Besides, we are able to estimate the flow flux in the upward and downward boundary layers from the steady state w_{max} and the HBL thickness. Figure 3.9 shows the time evolutions of w_{max} for three cases (j_{ave} [mA/cm^2], L [mm])=(2, 2), (2, 1), and (1, 2).

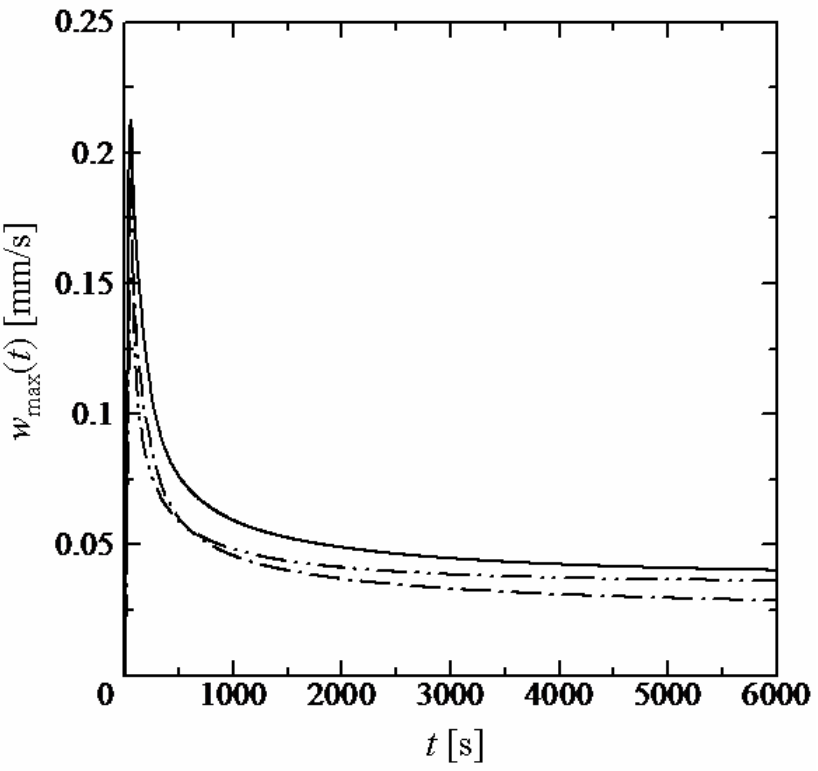

Figure 3.9: Time evolution of maximal free convective velocity w_{max} at z [mm]=5 for (j_{ave} [mA/cm^2], L [mm])=(2, 2) (solid line), (1, 2) (dashed-dotted line), and (2, 1) (dashed-two dotted line).

First we compare the peak values of w_{max} for same L but different j_{ave}, i.e. the solid and dashed- dotted lines. The peak value of w_{max} is about 0.155 mm/s at t [s]=72 for (1, 2), while it is about 0.21 mm/s at t [s]=54 for (2, 2). Thus, when L is fixed and j_{ave} increases, the peak value becomes larger and the corresponding peak time becomes earlier. This implies that as j_{ave} is larger, the gradient of the initial rise gets steeper. Next we note that the peak value of w_{max} is about 0.19 mm/s at t [s]=54 for (2, 1). Therefore, as L decreases, the peak value becomes smaller but the peak time hardly changes, so that the gradient of the initial rise becomes more moderate.

Concerning the approach to the steady state, we observe in Figure 3.9 that w_{max}

converges to the respective limit in all the three cases. By the use of the definition of the steady state introduced in the Section 3.2.1 (Page 35), we find $w_\infty = 0.0285$ mm/s at t [s]=5700 for (1, 2) and $w_\infty = 0.0365$ mm/s at t [s]=4800 for (2, 1). It is thus found that the steady state is attained earlier for smaller L.

In order to investigate the effect of the operational conditions on the nonuniformity of vertical current density distribution, we plot in Figure 3.10 the steady state cathodic current density distribution along the vertical direction for the above three cases.

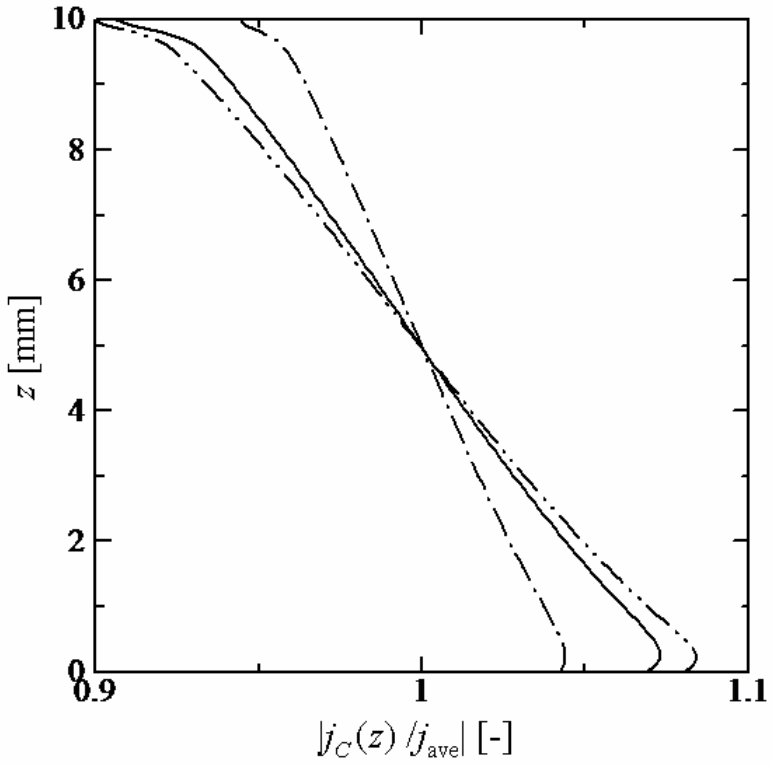

Figure 3.10: Steady state vertical current density distribution along the cathode surface for (j_{ave} [mA/cm^2], L [mm])=(2, 2) (solid line), (1, 2) (dashed-dotted line), and (2, 1) (dashed-two dotted line).

By comparing the vertical current density distributions for same L but different j_{ave}, i.e. the solid and dashed-dotted lines, we see that the current density distribution becomes more nonuniform in the z direction for larger j_{ave}. This dependence of the nonuniformity of current density distribution on j_{ave} is reasonable because the stronger rotational flow brings the heavier fluid from the anode side. It is consistent with the past experimental studies [16-22].

Next, we compare the vertical current density distributions for same j_{ave} but different L, i.e. the solid and dashed-two dotted lines. We find that the nonuniformity is stronger for smaller L. This result is not trivial because the shortening of L makes two opposite effects. One is to reduce the nonuniformity by weakening the swirling flow (Figure 3.9). The other is to enhance the nonuniformity by the reduction of molecular diffusion effect as shown below.

Figure 3.11 shows the contour of the steady state concentration profile for (j_{ave} [mA/cm^2], L [mm])=(2, 2) and (2, 1). It is seen that concentration diffusion in the vertical direction is larger for (2, 2). It is ascribed to the viscous effect and molecular diffusion over a long distance along the top and bottom wall surfaces. Thus, the enhancement of nonuniformity of current density distribution for smaller L obtained in the present case is understood as that the molecular diffusion effect dominates the change of magnitude of the swirling flow.

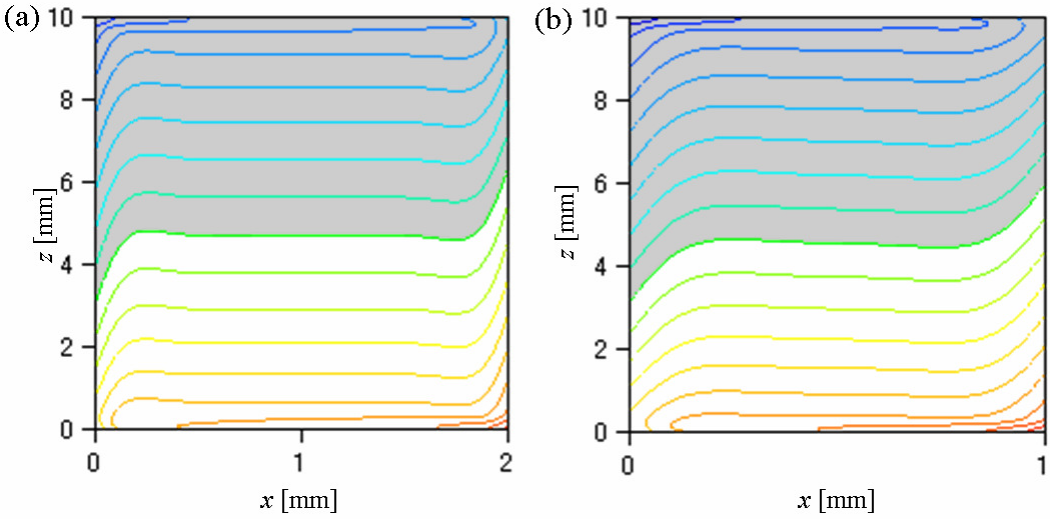

Figure 3.11: The contour of concentration profile at the steady state for (a) (j_{ave} [mA/cm^2], L [mm])=(2, 2), and (b) (2, 1). The region where the concentration is less than the initial value of 0.6 M is shaded. The contour interval is $m_0/30$.

Section 4 Concluding Remarks

We studied the development mechanism of vertical current density distribution on the electrode surface throughout the electrochemical reactions in confined electrochemical system. The concentration of $CuSO_4$ is depleted (or enriched) near the cathode (or anode) surface due to the electrochemical deposition (or dissolution) of copper on the surface. Because the fluid density increases with the concentration, the upward and downward convections develop along the cathode and anode surfaces, respectively. A swirling fluid motion compatible with the buoyant flow initially develops. At the same time, strong shear flows are formed along the top and bottom walls. After that, mass transfer by advection is clearly observed, and the vertical concentration diffusion process is then seen. At the final time of the present numerical simulation, the interior region is almost stagnant, whereas a boundary layer flow prevails along the electrode and wall surfaces of the container.

We confirmed by the Shanks transformation that the steady state electrolyte flow attained after a long-term decay period by viscous effect. At the steady state, a swirling boundary layer flow is observed along the electrode and wall surfaces. A heavier (or lighter) electrolyte solution is transferred to the lower cathode (or upper anode) region by this rotational flow. The supply of concentration from the counter electrode causes an extreme value in the vertical current density distribution. It is located in the lower cathode region, which is close to the maximum velocity point in the hydrodynamic boundary layer formed along the bottom wall surface. Mass transfer associated with the rotational flow promotes the vertically nonuniform current density distribution.

We investigated the dependence of the vertical nonuniformity of current density distribution on the operational electrolytic conditions such as the applied average current density j_{ave} and the electrode spacing L. When L is fixed and j_{ave} increases, current density distribution on the electrode surface becomes more nonuniform. This dependence of the nonuniformity of current density distribution on j_{ave} is reasonable because the stronger rotational boundary layer flow brings the heavier fluid from the anode side. By comparing the vertical current density distributions for same j_{ave} but different L, we saw that the nonuniformity was stronger for smaller L, even though the steady swirling flow got weaker. This result is not trivial because the shortening of L makes two opposite effects. One is to reduce the nonuniformity by weakening the rotational flow. The other is to enhance the nonuniformity by the reduction of molecular diffusion effect. We recognized that the enhancement of nonuniformity of current density distribution for smaller L obtained in this study was understood as that the molecular diffusion process dominated the change of the magnitude of swirling fluid motion.

The mathematical model developed in this thesis does not take the electrode shape evolution into account. However, the electrode surface roughness actually develops with the duration time of electrolysis. The growth rate of surface roughness is proportional to the current density, so that we consider the methodology described in this thesis as useful for further numerical study. However, it is still unsolved how to mathematically describe the surface roughness development as the moving boundary problem. The electrochemical deposition and dissolution mechanisms severely depend on the electrode surface condition and the degree of nonequilibrium. The

recent progress in micro- and nano-scale experimental setups may provide much helpful information to model the surface roughness development.

The comparison to the real physicochemical phenomena is indispensable to develop more realistic and sophisticated model equation and boundary condition. Certainly it is quite difficult to figure out the complete picture of physicochemical hydrodynamic phenomena in the actual electrochemical experiment. But we are able to measure and observe the local characteristic mass transfer and flow structures. Repetition of numerical experiment and subsequent comparison to measurement of the real electrochemical phenomena accumulates the know-how. It may lead further improvement of mathematical model. The author believes that methodology and calculated results in the present study contribute to more realistic numerical modeling in electrochemical system.

List of Publications

S. Kawai, K. Nishikawa, Y. Fukunaka, and S. Kida

"Numerical simulation of transient natural convection induced by electrochemical reactions confined between vertical plane Cu electrodes"

Electrochim. Acta, **53**, 257-264 (2007).

S. Kawai, Y. Fukunaka, and S. Kida

"Numerical Simulation of Transient Natural Convection along Vertical Plane Electrodes Caused by Electrolytic Current Modulation"

J. Electrochem. Soc., **155**, F75-F81 (2008).

S. Kawai, Y. Fukunaka, and S. Kida

"Numerical Simulation of Coupling Phenomena between Ionic Mass Transfer Rate and Morphological Variations of Electrodeposited Copper "

J. Jpn. Soc. Microgravity Appl., **25**, 3, 521-526 (2008).

S. Kawai, Y. Fukunaka, and S. Kida

"Numerical Simulation of Ionic Mass Transfer Rates with Natural Convection in $CuSO_4$-H_2SO_4 Solution Part I. Numerical Study on the Developments of Secondary Flow and Electrolyte Stratification Phenomena"

J. Electrochem. Soc., **156**, F99-F108 (2009).

S. Kawai, Y. Fukunaka, and S. Kida

"Numerical Simulation of Ionic Mass Transfer Rates with Natural Convection in $CuSO_4$-H_2SO_4 Solution Part II. Comparisons Between Numerical Calculations and Optical Measurements"

J. Electrochem. Soc., **156**, F109-F114 (2009).

S. Kawai, K. Nishikawa, Y. Fukunaka, and S. Kida

"Numerical Simulation of Ionic Mass Transfer Phenomena Accompanying Electrochemical Reactions in PC and Ionic Liquid"

Electrochemistry, **77**, 8, 601-603 (2009).

S. Kawai, Y. Fukunaka, and S. Kida

"Ionic Mass Transfer Rate Accompanying Pulsed Current Electrodeposition of Silver"

submitted to Transactions of Materials Research Society of Japan

I. Arise, S. Kawai, Y. Fukunaka, and F. R. McLarnon

"Numerical Calculation Ionic Mass Transfer Rates Accompanying Anodic Zinc Dissolution in Alkaline Solution"

submitted to J. Electrochem. Soc.

S. Kawai, Y. Fukunaka, and S. Kida

"Numerical Calculation of Transient Current Density Distribution along Vertical Plane Electrode in $CuSO_4$-H_2SO_4 Electrolyte Solution"

submitted to J. Electrochem. Soc.

S. Kawai, Y. Fukunaka, and S. Kida

"Transient Mass Transfer Rate of Cu^{2+} Ion Caused by Copper Electrodeposition with Alternating Electrolytic Current"

submitted to Electrochim. Acta

Acknowledgements

The author is sincerely grateful to Prof. S. Kida for his careful supervision and continuous encouragement throughout this study.

The author would like to thank Prof. H. Hanazaki for his valuable suggestions and comments. The author wishes to thank Dr. S. Goto for his valuable suggestions and continuous encouragement.

Special thanks are due to Prof. Y. Fukunaka for his valuable suggestions, discussion and continuous encouragement throughout this study based on his profound understanding of electrochemistry. He imparted basic and specialized knowledge to the author.

The author wishes to express his acknowledgement to Prof. T. Matsuoka, Prof. A. Ueda, and Prof. C. R. Miranda for their continuous support. The author wishes to thank Dr. M. C. Lafouresse for her valuable suggestions.

The author would like to thank Prof. R. C. Alkire and Prof. P. C. Searson for their valuable discussion and effective advices.

The author wishes to express his acknowledgement to Prof. T. Nohira, Prof. T. Goto, and Dr. H. Matsushima for their helpful advices and kind encouragements. Special thanks are due to Dr. M. Motoyama and Dr. K. Nishikawa for their valuable discussion and warm and continuous encouragements throughout this study. The author would like to thank Messers I. Arise and T. Nishida for their kind cooperation and warm encouragements.

The author extends a special thank you to all people in fluid mechanics

research group, space energy and resources group, laboratory of engineering geology, and energy resources engineering group for their kind help and support. The author has learned a lot of things from their discussion and talking.

Finally, the author is always grateful to his family for continuous support and encouragement.

References

[1] P. C. Andricacos, C. Uzoh, J. O. Dukovic, J. Horkans, and H. Deligianni, *I.B.M. J. Res. Develop.*, **42** 567-574 (1998).

[2] T. M. Whitney, J. S. Jiang, P. C. Searson, and C. L. Chien, *Science*, **261** 1316-1319 (1993).

[3] C. R. Martin, *Science*, **266** 1961-1966 (1994).

[4] H. Masuda, and K. Fukuda, *Science*, **268** 1466-1468 (1995).

[5] R. D. Braatz, R. C. Alkire, E. Seebauer, E. Rusli, R. Gunawan, T. O. Drews, X. Li, and Y. He, *J. Process Control*, **16** 193-204 (2006).

[6] A. K. Biswas, and W. G. Davenport, "Extractive Metallurgy of Copper", Third Edition, Pergamon Press (1994).

<6-a>: Page 324-354, Chapter 17 "Electrolytic Refining of Copper".

<6-b>: Page 401-412, Chapter 20 "Electrowinning".

[7] M. Stelter, and H. Bombach, *Adv. Eng. Mater.* **2004**, 6 558-562.

[8] M. Hayase, and N. Nagao, *J. Electrochem. Soc.*, **156** D198-D203 (2009).

[9] W.-P. Dow, C.-C. Li, Y.-C. Su, S.-P. Shen, C.-C. Huang, C. Lee, B. Hsu, and S. Hsu, *Electrochim. Acta.*, **54** 5894-5901 (2009).

[10] W.-P. Dow, M.-Y. Yen, S.-Z. Liao, Y.-D. Chiu, and H.-C. Huang, *Electrochim. Acta.*, **53** 8228-8237 (2008).

[11] S. H. Cha, S.-S. Kim, S. K. Cho, and J. J. Kim, *Electrochem. Solid-State Lett.*, **10** D22-D24 (2007).

[12] D. Wheeler, D. Josell, and T. P. Moffat, *J. Electrochem. Soc.*, **150** C302-C310 (2003).

[13] D. Josell, B. Baker, C. Witt, D. Wheeler, and T. P. Moffat, *J. Electrochem. Soc.*, **149** C637-C641 (2002).

[14] T. P. Moffat, J. E. Bonevich, W. H. Huber, A. Stanishevsky, D. R. Kelly, G. R. Stafford, and D. Josell, *J. Electrochem. Soc.*, **147** 4524-4535 (2000).

[15] K. M. Takahashi, and M. E. Gross, *J. Electrochem. Soc.*, **146** 4499-4503 (1999).

[16] C. Wagner, *J. Electrochem. Soc.*, **95** 161-173 (1949).

[17] K. Asada, F. Hine, S. Yoshizawa, and S. Okada, *J. Electrochem. Soc.*, **107** 242-246 (1960).

[18] J. R. Lloyd, E. M. Sparrow, and E. R. G. Eckert, *J. Electrochem. Soc.*, **119** 702-707 (1972).

[19] J. R. Lloyd, E. M. Sparrow, and E. R. G. Eckert, *Int. J. Heat Mass Transfer.*, **15** 457-473 (1972).

[20] Y. Awakura, A. Ebata, and Y. Kondo, *J. Electrochem. Soc.*, **126** 23-30 (1979).

[21] Y. Konishi, Y. Tanaka, Y. Kondo, and Y. Fukunaka, *Electrochim. Acta.*, **46** 681-690 (2000).

[22] N. Ibl, W. Ruegg, and G. Trumpler, *Helv. Chim. Acta.*, **36** 1624-1630 (1953).

[23] C. R. Wilke, M. Eisenberg, and C. W. Tobias, *J. Electrochem. Soc.*, **100** 513-523 (1953).

[24] A. Eklund, F. Alavyoon, D. Simonsson, R. I. Karlsson, and F. H. Bark, *Electrochim. Acta.*, **36** 1345-1354 (1991).

[25] F. Alavyoon, A. Eklund, F. H. Bark, R. I. Karlsson, and D. Simonsson, *Electrochim. Acta.*, **36** 2153-2164 (1991).

[26] P. Olivas, S. Zahrai, and F. H. Bark, *J. Appl. Electrochem.*, **27** 1369-1379 (1997).

[27] M. Georgiadou, R. Mohr, and R. C. Alkire, *J. Electrochem. Soc.*, **147** 3021-3028

(2000).

[28] Ph. Mandin, C. Fabian, and D. Lincot, *J. Electrochem. Soc.*, **153** D40-D50 (2006).

[29] J. Newman, “Electrochemical Systems”, Prentice-Hall, Inc., Englewood Cliffs, NJ (1973).

<29-a>: Page 317-334, Chapter 13 “THERMAL EFFECTS”.

<29-b>: Page 171-202, Chapter 7 “STRUCTURE OF THE ELECTRIC DOUBLE LAYER”.

<29-c>: Page 271-296, Chapter 11 “INFINITELY DILUTE SOLUTIONS”.

<29-d>: Page 2-4, “1.1 Thermodynamics and Potential”.

<29-e>: Page 4-7, “1.2 Thermodynamics and Potential” and “1.3 Kinetics and Rates of Reaction”.

<29-f>: Page 203-240, Chapter 8 “ELECTRODE KINETICS”.

[30] I. Rubinstein, “Electro-Diffusion of Ions”, Society for Industrial and Applied Mathematics, SIAM, Philadelphia (1990).

<30-a>: Page 1-22, Chapter 1 “Introduction”.

[31] E. M. Sparrow, and J. L. Gregg, *Trans*. ASME, **78** 435-440 (1956).

[32] S. W. Churchill, and H. Ozoe, *Trans*. ASME, C-**95**, 3 540-541 (1973).

[33] J. R. Selman, and J. Newman, *Trans*. ASME, C-**93**, 4 465-466 (1971).

[34] J. R. Selman, and C. W. Tobias, *J. Electroanal. Chem.*, **65** 67-85 (1975).

[35] J. R. Selman, and J. Tavakoli-Attar, *J. Electrochem. Soc.*, **127** 1049-1055 (1980).

[36] M. Eisenberg, C. W. Tobias, and C. R. Wilke, *J. Electrochem. Soc.*, **103** 413-416 (1956).

[37] Y. Awakura, and Y. Kondo, *J. Electrochem. Soc.*, **123** 1184-1192 (1976).

[38] N. Ibl, and R. H. Muller, *J. Electrochem. Soc.*, **105** 346-353 (1958).

[39] Y. Awakura, Y. Takenaka, and Y. Kondo, *Electrochim. Acta.*, **21** 789-797 (1976).

[40] Y. Fukunaka, T. Minegishi, N. Nishioka, and Y. Kondo, *J. Electrochem. Soc.*, **128** 1274-1280 (1981).

[41] Y. Fukunaka, K. Denpo, M. Iwata, K. Maruoka, and Y. Kondo, *J. Electrochem. Soc.*, **130** 2492-2499 (1983).

[42] K. Denpo, T. Okumura, Y. Fukunaka, and Y. Kondo, *J. Electrochem. Soc.*, **132** 1145-1150 (1985).

[43] E. Mattsson, and J. O'M. Bockris, *Trans. Faraday Soc.,* **55** 1586-1601 (1959).

[44] J. O'M. Bockris, and H. Kita, *J. Electrochem. Soc.,* **109** 928-939 (1962).

[45] O. R. Brown, amd H. R. Thirsk, *Electrochim. Acta.*, **10** 383-393 (1965).